Geophys. J. Int. (0000) **000**, 000–000

Parsimonious Refraction Interferometry

Sherif Hanafy[1]* Gerard T. Schuster[1]

[1]*Department of Earth Science and Engineering, King Abdullah University of Science and Technology, Saudi Arabia*

**E-mail: sherif.geo@gmail.com*

24 September 2016

SUMMARY

We present parsimonious refraction interferometry where a densely populated refraction data set can be obtained from several reciprocal and infill shot gathers. The assumptions are that the first arrivals consist of head waves and direct waves, and a pair of reciprocal shot gathers and several infill shot gathers are recorded over the line of interest. Refraction traveltimes from these shot gathers are picked and spawned into $O(N^2)$ refraction traveltimes generated by N virtual sources, where N is the number of geophones in the 2D survey. This enormous increase in the number of traveltime picks and associated rays, compared to the many fewer traveltimes from the reciprocal and infill shot gathers, allows for increased model resolution and a better condition number with the system of normal equations. A significant benefit is that the suggested survey and the associated traveltime picking is far less time consuming than that for a standard refraction survey with a dense distribution of sources.

1 INTRODUCTION

Refraction tomography is an important imaging tool in earthquake studies (Stein and Wyession, 2003), crustal-mantle imaging (Prodehl and Mooney, 2012), exploration geophysics (Bishop et al., 1985; Yilmaz, 2001), and engineering seismology (Yilmaz, 2015). For 2D engineering seismology, receivers are deployed along a line and common shot gathers (CSGs) are recorded for source positions at selected positions on

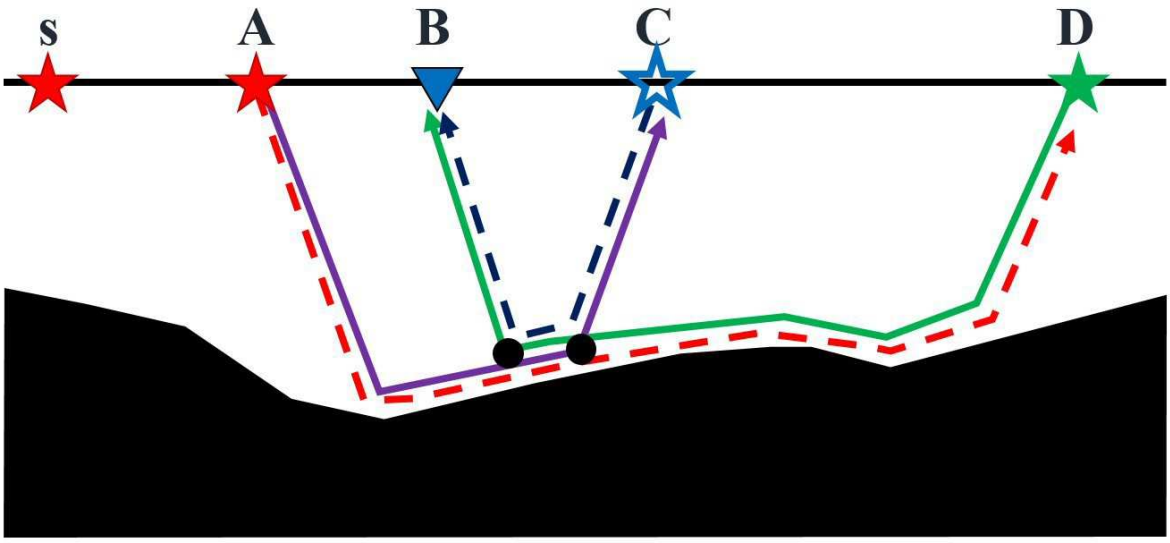

Figure 1. Two-layer model where the black medium is faster than the top layer; the reciprocal sources are at **A** and **D** and are associated with the dashed red ray. The dashed blue raypath is associated with the virtual refraction ray that is excited by the virtual source (blue star) at **C** and terminates at **B**. The refraction traveltimes associated with the reciprocal shots (green and red stars) can be decomposed into the virtual refraction traveltime generated by the blue star.

the line. To save costs, a parsimonious survey is carried out where sources are located only at each end of the receiver line in Figure 1. The first breaks are picked from each shot gather and the traveltimes are inverted by a simple formula that assumes a layered medium with an unknown dip angle for each interface. These two shot gathers are denoted as a pair of reciprocal shot gathers. We often require several short-offset infill shot gathers that can be used to find the near-offset traveltimes. Therefore, parsimonious surveys can significantly reduce acquisition costs and survey efforts, but at the cost of less slowness resolution and certainty in the estimate of the subsurface model.

For a 2D survey, we now show that two reciprocal shot gathers and several short-offset infill shot gathers can be decomposed into many virtual-shot gathers that have many more traveltime picks available for inversion. In some cases, the virtual-shot gathers give as much refraction information as a full survey with N shots, where a shot is located at each of the N geophone locations. The result is a tomogram with a much denser ray coverage and better slowness resolution compared to that from the original data. We call this procedure parsimonious interferometry because it uses a stationary-phase principle to decompose the reciprocal traveltimes into many virtual traveltimes associated with shorter raypaths. Unlike the original pair of reciprocal shots, the virtual-shot locations are at all of the interior geophone locations.

The next section describes the theory of parsimonious refraction interferometry. It is a special case of Fermat's interferometric traveltime principle (Schuster, 2005) and closure phase (Schuster et al., 2014) that allows for the decomposition of long raypaths and traveltimes into, respectively, shorter raypaths and traveltimes. Instead of body-wave traveltimes we now apply it to head-wave traveltimes. Section 3 presents the results of applying parsimonious interferometry to both synthetic data and field data. The field data are from 2D surveys conducted next

to the Gulf of Aqaba, near King Abdullah University of Science and Technology (KAUST), and over a basin in East Africa. The final section presents a summary and conclusions.

2 THEORY

Assume two reciprocal sources and the irregularly layered medium in Figure 1, where head waves propagate along the interface between the upper and lower layers. There can be lateral velocity variations in the upper medium and there are N evenly spaced geophones on the recording surface between the two sources. The head-wave traveltime from the source at $\mathbf{A}$ to the geophone at $\mathbf{C}$ is defined as

$$\tau_{AC} \quad = \quad \tau_{Ax'} + \tau_{x'x} + \tau_{xC}, \tag{1}$$

and the reciprocal traveltime from $\mathbf{D}$ to $\mathbf{B}$ is

$$\tau_{DB} \quad = \quad \tau_{Dx} + \tau_{xx'} + \tau_{x'B}, \tag{2}$$

where $\tau_{xx'}$ is the traveltime from $\mathbf{x}$ to $\mathbf{x}'$ along the refraction ray, and reciprocity says $\tau_{xx'} = \tau_{x'x}$. The traveltimes τ_{AC} and τ_{DB} are denoted as a pair of reciprocal traveltimes.

2.1 Virtual-Traveltime Equation

To create virtual sources and receivers within the array in Figure 1, we assume that there is a postcritical distance between the geophone positions $\mathbf{C}$ and $\mathbf{B}$ and both traveltimes τ_{AC} and τ_{DB} are associated with the same refractor. Subtracting the reciprocal traveltime $\tau_{AD} = \tau_{Ax'} + \tau_{x'x} + \tau_{xD}$ from the sum $\tau_{AC} + \tau_{DB}$ gives the virtual traveltime $\delta\tau_{CB}$:

$$\begin{aligned}
\delta\tau_{CB} \quad &= \quad \tau_{AC} + \tau_{DB} - \tau_{AD}, \\
&= \quad \tau_{Ax'} + \tau_{x'x} + \tau_{xC} + [\tau_{Dx} + \tau_{xx'} + \tau_{x'B}] - \tau_{Ax'} - \tau_{x'x} - \tau_{xD}, \\
&= \quad \tau_{Cx} + \tau_{xx'} + \tau_{x'B}.
\end{aligned} \tag{3}$$

$\delta\tau_{CB}$ is denoted as an interferometric stationary traveltime because the reciprocal raypath $\overline{Ax'xD}$, marked by the dashed red ray in Figure 1, cancels the phase associated with the common raypaths of the purple $\overline{Ax'xC}$ and green $\overline{Dxx'B}$ rays. The result is the virtual traveltime $\delta\tau_{CB}$ associated with the much shorter raypath $\overline{Cxx'B}$ denoted by the dashed blue ray. Equivalently, $\delta\tau_{CB}$ is the traveltime of a virtual refraction excited by a virtual source at $\mathbf{C}$ and recorded at $\mathbf{B}$. This natural redatuming operation is the key principle underlying seismic interferometry (Snieder, 2004; Wapenaar, 2004).

Equation 3 can be used to generate $O(N)$ virtual-shot gathers of head-wave traveltimes, where the number of reciprocal geophone pairs with postcritical separation is assumed to be nearly equal to the number N of geophones in the survey. Each virtual-shot gather will, on

average, contain $O(N)$ virtual traveltimes to create $O(N^2)$ virtual refraction traveltimes from the $2N$ traveltimes picked from two reciprocal shot gathers. This abundance of new traveltimes can be used to invert for the subsurface velocity model with much greater ray density and better model resolution than inverted from the original data set.

Equation 3 satisfies Fermat's interferometric principle (Schuster, 2005) because the subtraction of τ_{AD} (red dashed ray) from $\tau_{AC}+\tau_{DB}$ (solid green and purple rays) gives the same value of $\delta\tau_{CB}$ for all postcritical, i.e. stationary, locations of the reciprocal sources. Equation 3 is also a special case of the closure phase condition discussed in (Schuster et al., 2014).

2.2 Condition Number, Illumination Area, and Slowness Uncertainty

The resolution properties associated with the virtual-traveltime equations are now compared to those from the reciprocal traveltime equations. These properties are 1) condition number of the normal equations, 2) the enhancement of illumination with virtual-traveltime equations, and 3) the slowness uncertainty associated with errors in traveltime picking.

Condition Number. As Appendix I shows, the extra traveltime equations generated by equation 3 act as a preconditioner that reduces the condition number of the normal matrix $[\mathbf{L}^T\mathbf{L}]$ by a factor of 3, where $\mathbf{L}$ is the raypath matrix associated with the traveltime equations. The dense set of virtual traveltimes does not create new information about the subsurface because it is created by adding and subtracting traveltime equations from the reciprocal data. However, the synthetic examples in the next section suggest that the enhanced subsurface illumination and smaller condition number in the virtual $\mathbf{L}^T\mathbf{L}$ matrix can significantly reduce the size of the null space solutions.

Illumination Zones and Spatial Resolution.

Figure 2a shows that a reciprocal pair of shot gathers can give rise to gaps in the illumination zones of the direct arrivals and refractions. For refractions, these gaps can be caused by the inability to pick far-offset traveltimes as indicated by the truncated green lines in Figure 2a. This problem can be partly remedied if the later-arriving direct waves and refractions can be picked, as illustrated by the dashed lines in Figure 2b. In practice, however, such picking is not an easy task.

A large illumination zone does not necessarily mean a good spatial resolution limit dx. Here, dx is the minimum width of a slowness box whose velocity can be resolved from the data. For virtual data dx depends on the midpoint position and minimum offset between a reciprocal pair of geophones. As an example, the pair of dashed vertical lines at A and B in Figure 2a indicates the reciprocal refraction traveltimes with minimum offset $dx = |x_A - x_B|$ that are pickable from the leftgoing and rightgoing refractions. This means that picking later refraction arrivals in Figure 2b will lead to wider subsurface illumination, but the estimated velocity model can still suffer from poor resolution as demonstrated by the wide double-sided black arrow. If both the first-arrival and later-arrival refraction times can be picked

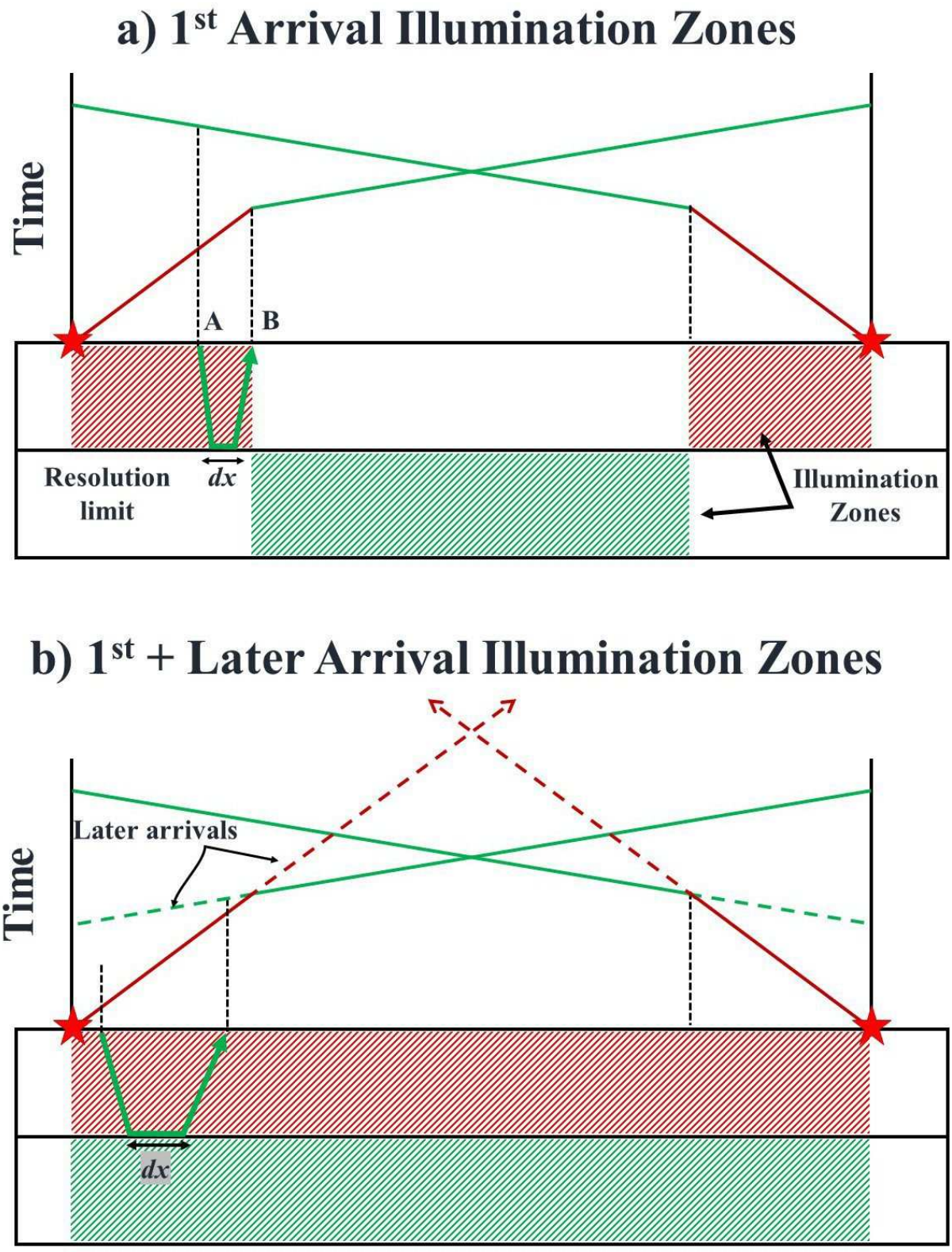

Figure 2. Hatched illumination zones for traveltimes picked from a) first arrivals and b) both first and the dashed later arrivals. The red (green) lines indicate direct-wave (refraction) arrivals. The horizontal resolution limit dx is denoted by black two-sided arrows for different portions of the subsurface. The resolution limit dx cannot be less than the distance between adjacent geophones.

almost everywhere between the two reciprocal shots, then the spatial resolution dx is equal to the spacing between adjacent geophones. This assumes that the typical wavelength of the arrivals is much shorter than a geophone spacing.

Slowness Variance.

Traveltime picking is prone to random errors, and so the variance Σ^2 of these data errors give rise to an uncertainty in the estimated slowness model, denoted by the slowness variance σ_i^2 in the i^{th} cell. Appendix II shows that the slowness variance associated with the reciprocal data is proportional to $\frac{1}{l^2}$, while that for the virtual data is proportional to $\frac{2}{Nl^2}$. Thus, the variance of the virtual slowness can be much less than that for the reciprocal data if N is large and there is only weak correlation in the data errors.

2.3 Consistency Test

A consistency test is now described which checks the validity of the assumption that the recorded refraction arrivals are those of head waves.

Assume head wave arrivals in Figure 3a so that

$$\bar{\tau}_{BC} \quad = \quad \tau_{B'C} + \tau_{C'B} - \tau_{B'C'}, \tag{4}$$

is the traveltime of a virtual head wave excited at $\mathbf{B}$ and recorded as a 1st-arrival at $\mathbf{C}$. However, this might not be a head-wave traveltime if the source at $\mathbf{A}$ is far from the receivers and there is a velocity gradient linearly increasing in depth. As an example, Figure 3b shows a diving wave recorded as a 1st-arrival at $\mathbf{B}$, $\mathbf{C}$, and $\mathbf{D}$ when there is a strong velocity gradient that linearly increases in depth. Diving waves violate the head-wave assumption underlying equation 4 so the resulting traveltime $\bar{\tau}_{BC}$ is that of an unphysical diving wave between $\mathbf{B}$ and $\mathbf{C}$ (see the dotted black ray in Figure 3b).

Therefore, traveltimes from recorded shot gathers must be tested for consistency with the head-wave assumption. We propose a consistency test identical to that given in (Dong et al., 2006) where the traveltimes of a common geophone pair gather (CPG) must equal one another if they are for head waves. As an example, the head-wave traveltimes in Figures 4a-c are transformed by

$$\bar{\tau}_{BC} \quad = \quad \tau_{AC} - \tau_{AB}, \tag{5}$$

into the traveltimes $\bar{\tau}_{BC}$ for the traces in Figures 4d. If the difference between these traveltimes is greater than the picking uncertainty for different positions of $\mathbf{A}$ on the leftside of $\mathbf{B}$ then they should be rejected as head-wave traveltimes associated with the same refractor.

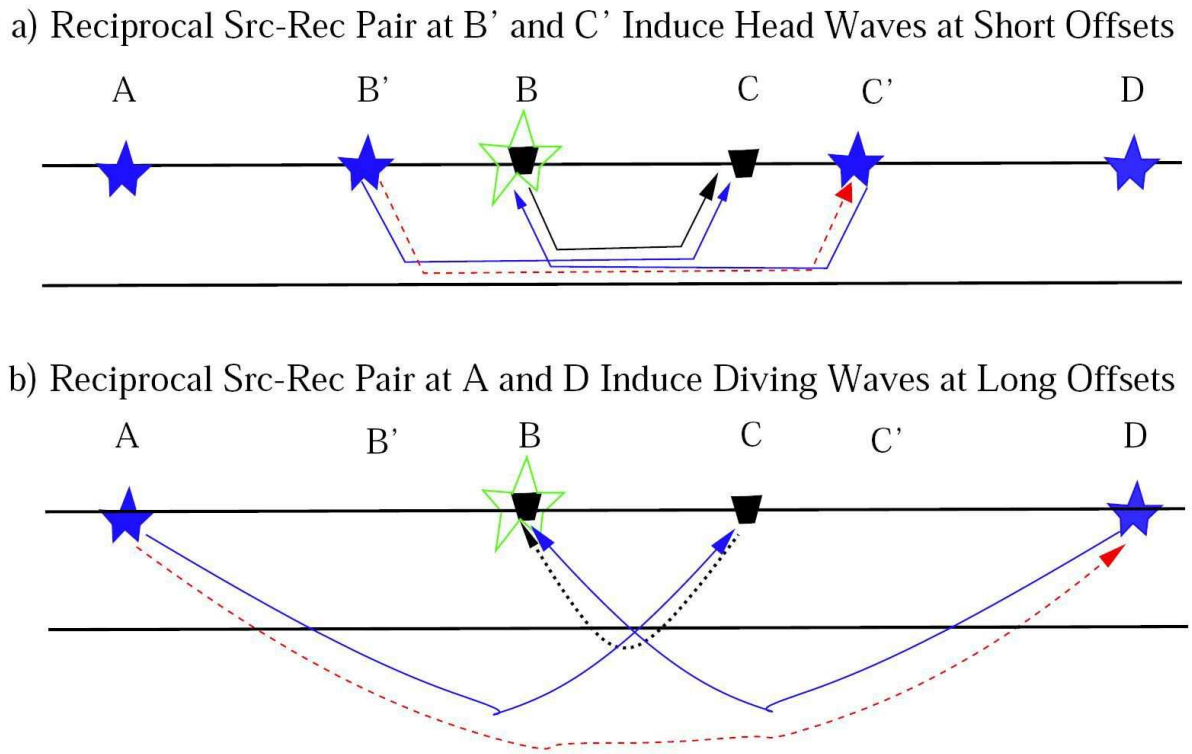

Figure 3. Virtual traveltimes created with a) short-offset $T_{BC} = T_{B'C} + T_{BC'} - T_{B'C'}$ and b) long-offset $\bar{T}_{BC} = T_{AC} + T_{DB} - T_{AC}$ virtual traveltimes. The long-offset (short-offset) sources generate diving waves (head waves) as first arrivals so that $T_{BC} \neq \bar{T}_{BC}$. The black solid ray corresponds to the virtual raypath associated with either T_{BC} or $\bar{T}_{BC}$.

3 NUMERICAL RESULTS

Parsimonious interferometry will be tested for traveltimes generated for three synthetic models and three seismic field surveys. One of the synthetic models is a three-layered velocity model with velocity gradient, the second is a complicated velocity model extracted from a field data tomogram, and the third has a strong velocity gradient that increases with depth to demonstrate the diving wave problem. In each synthetic case the traveltimes were generated using a finite-difference solution to the eikonal equation (Qin et al., 1992) and inverted by the multiscale gradient method described in (Nemeth et al., 1997). The field examples are for refraction data recorded near the Gulf of Aqaba, over a wadi near KAUST, and over a deep basin in East Africa.

3.1 Three-Layer Synthetic Model

The three-layer model shown in Figure 5a contains 3 layers, the first one has a constant velocity of 400 m/s, the second one has a horizontal velocity gradient of 0.2 m/s/m, while the third layer has a vertical velocity gradient of 4 m/s/m with a minimum velocity value of 2600 m/s. A finite-difference solution (Qin et al., 1992) to the 2D eikonal equation is used to compute 240 shot gathers of first-arrival traveltimes (Figure 6a), where the source and receiver points are located every 5 m on the surface.

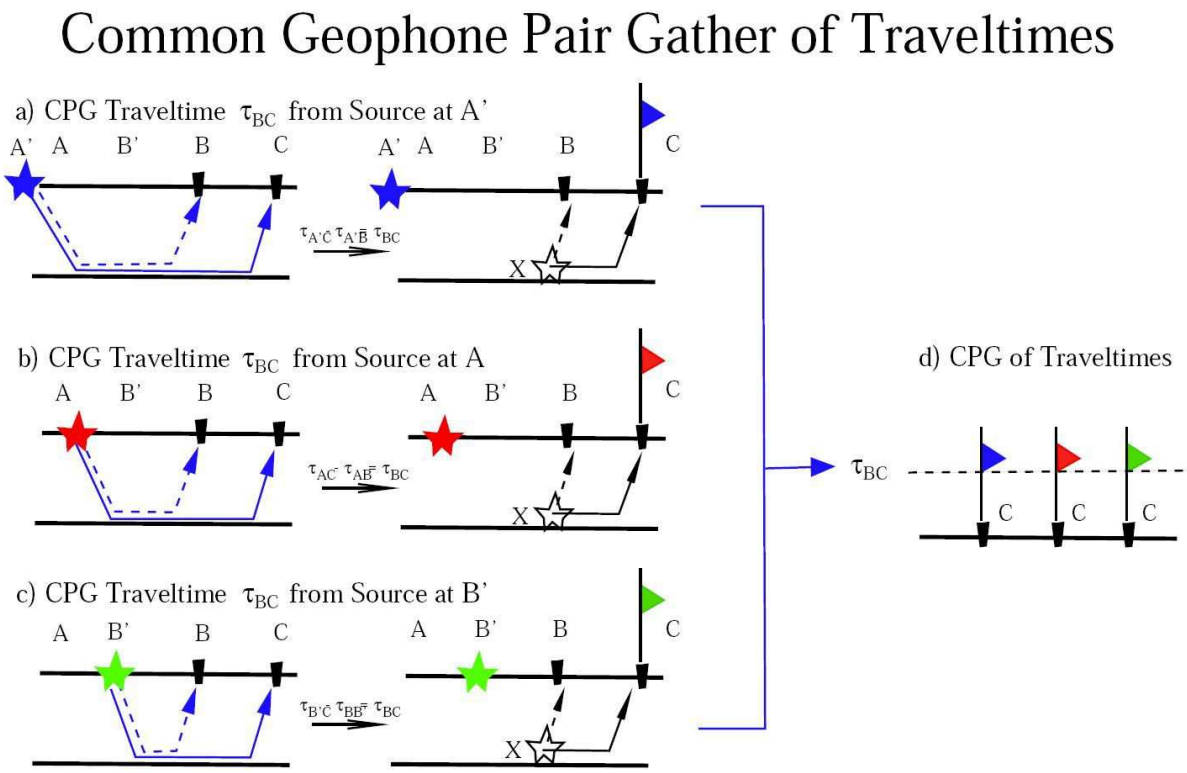

Figure 4. Virtual traveltimes τ_{BC} created by computing a) $\tau_{A'C} - \tau_{A'B}$, b) $\tau_{AC} - \tau_{AB}$, and c) $\tau_{B'C} - \tau_{B'B}$. If the input traveltimes are those of head waves, then the output d) traveltime τ_{BC} will be that of a virtual head wave recorded at C. The common geophone pair gather (CPG) of virtual traces in a-c share the same pair of geophones at $\mathbf{B}$ and $\mathbf{C}$, but have different source locations.

The two reciprocal shot gathers contain 480 first-arrival traveltimes, where one source is at $(0, 0)$ and the other is at $(1200, 0)$ in addition to 5 infill shot gathers with only near-offset traces (Figure 6b) are inverted by traveltime tomography to get the reciprocal tomogram in Figure 5b. In this case there is a poor correspondence between the reciprocal tomogram and the actual velocity model. For comparison, Figure 5c shows the standard tomogram inverted from the $actual$ traveltimes generated by exciting shots at each of the 240 geophones. As expected, the standard tomogram mostly agrees with the actual velocity model.

Equation 3 is then used to compute the virtual traveltimes from the 480 traveltimes associated with the two reciprocal shot gathers. To account for the fact that the direct-wave traveltimes could not be generated at long offsets, the direct-wave traveltimes were picked from 5 infill CSGs with the shots evenly located at 200 m intervals between the endpoints of the receiver line. These direct-wave traveltimes were then interpolated to other source locations to fill in the missing direct-wave traveltimes in the other CSGs. The result is the creation of $O(57,000)$ virtual traveltimes computed for virtual shots at each of the geophones (Figure 6c). These virtual traveltimes are inverted to give the virtual tomogram shown in Figure 5d. This tomogram agrees with the standard tomogram, which is not surprising because (1) the virtual traveltimes match the true traveltimes as shown in Figures 6d and 7a, (2) there are few diving waves in the model, and (3) there is a dense

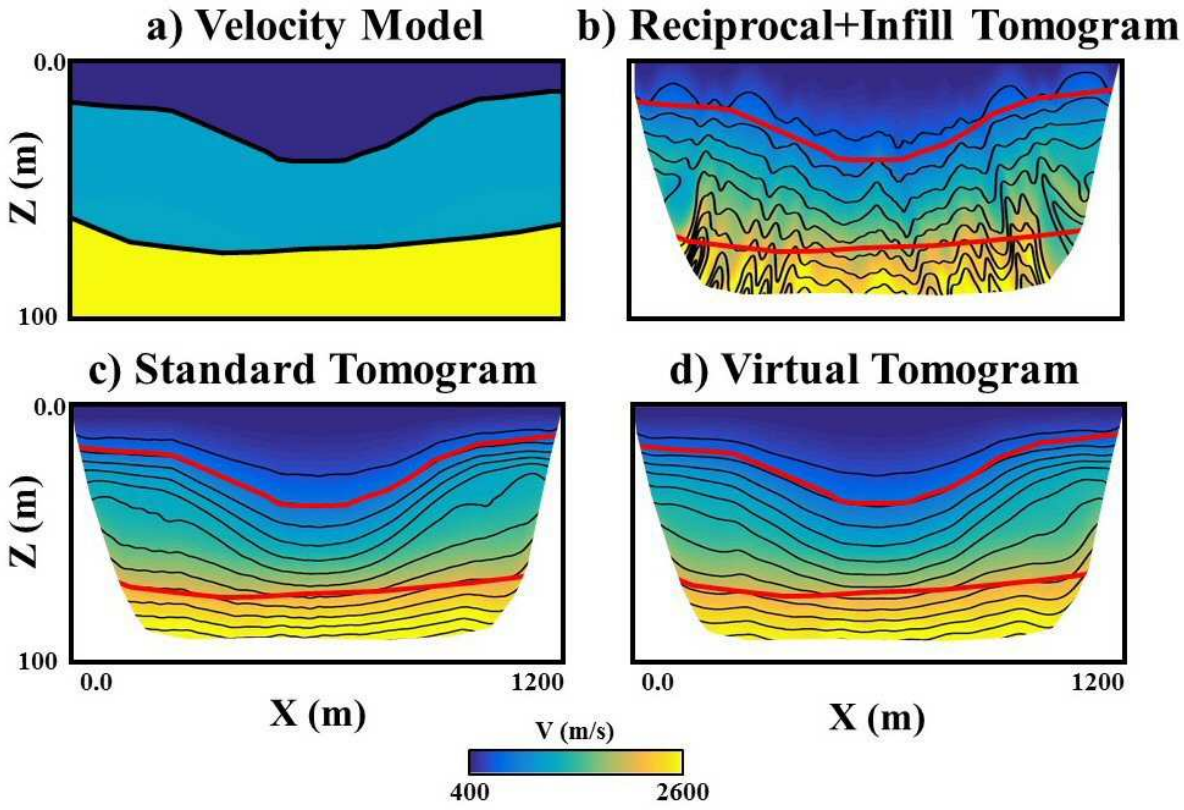

Figure 5. a) Three-layer model, b) reciprocal tomogram inverted from the the two reciprocal and 5 infill shot gathers, c) standard tomogram inverted from the 57,600 actual traveltimes in 240 shot gathers, with a shot at each geophone location. d) Virtual tomogram inverted from $O(57,000)$ virtual traveltimes created from reciprocal and 5 infill traveltimes.

illumination in the subsurface from the virtual rays. These results could have been predicted by determining whether or not the traveltimes in the CPGs are flat. Figure 8a shows that the CPG traveltimes mostly agree with one another for the same CPG.

3.2 Aqaba Synthetic Model

Parsimonious interferometry is also tested on the Aqaba velocity model in Figure 9a, which is based on a tomogram computed from data recorded near the Gulf of Aqaba. In this example, first arrival traveltimes of 120 shot gathers each has 120 receivers are computed by a finite-difference solution to the eikonal equation (Figure 10a). Here, the shot and receiver intervals are 5 m. The input data consist of traveltimes from two reciprocal shot gathers (240 traveltimes) and 5 infill shot gathers with the shots evenly located at 60 m intervals between the endpoints of the receiver line; each shot gather has 30 near-offset receivers (Figure 10b). Both the reciprocal and infill direct-wave traveltimes were inverted to give the Figure 9b tomogram. As expected there is a poor correspondence between this tomogram and the velocity model. In this case the input data consists of 120 traveltimes in each reciprocal shot gather and 277 traveltimes from the infill shot gathers, which gives a total of 517 traveltimes.

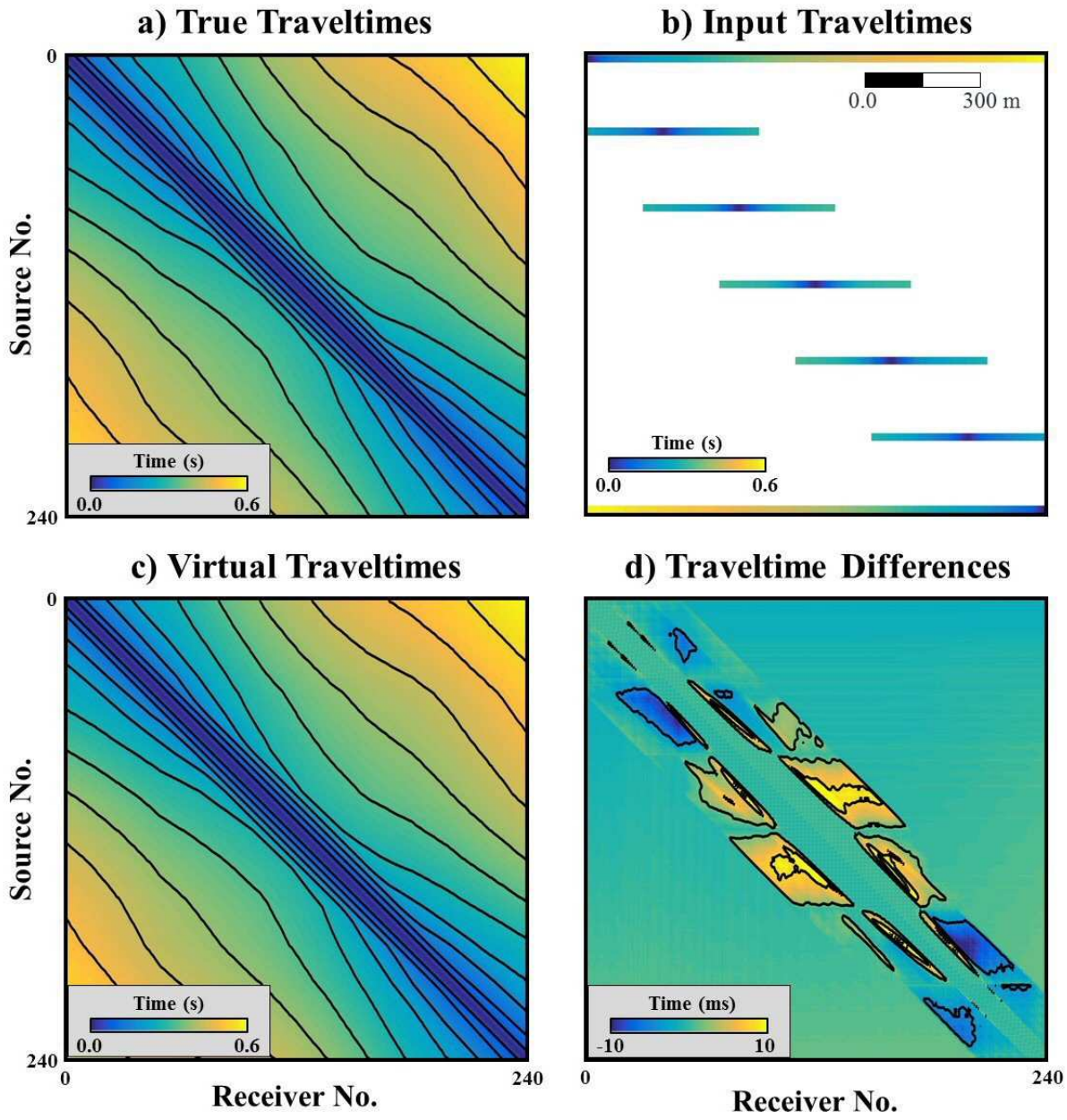

Figure 6. a) The actual trvaeltime picks, b) two reciprocal and 5 infill shot gathers used as input to the proposed method, c) the virtual traveltimes calculated from equation 3, and d) the difference between the actual and the virtual traveltime picks.

The traveltimes of the $120^2 = 14,400$ actual traveltimes are inverted to give the standard P-velocity tomogram in Figure 9c. This tomogram shows a much better correspondence with the actual velocity model than seen in the reciprocal tomogram.

Equation 3 was then used to compute $14,400$ virtual traveltimes. Some of these traveltimes are not physically related to refraction times because the receiver-receiver offset is not at a post-critical offset. Such non-physical traveltimes are identified by a sudden change in the

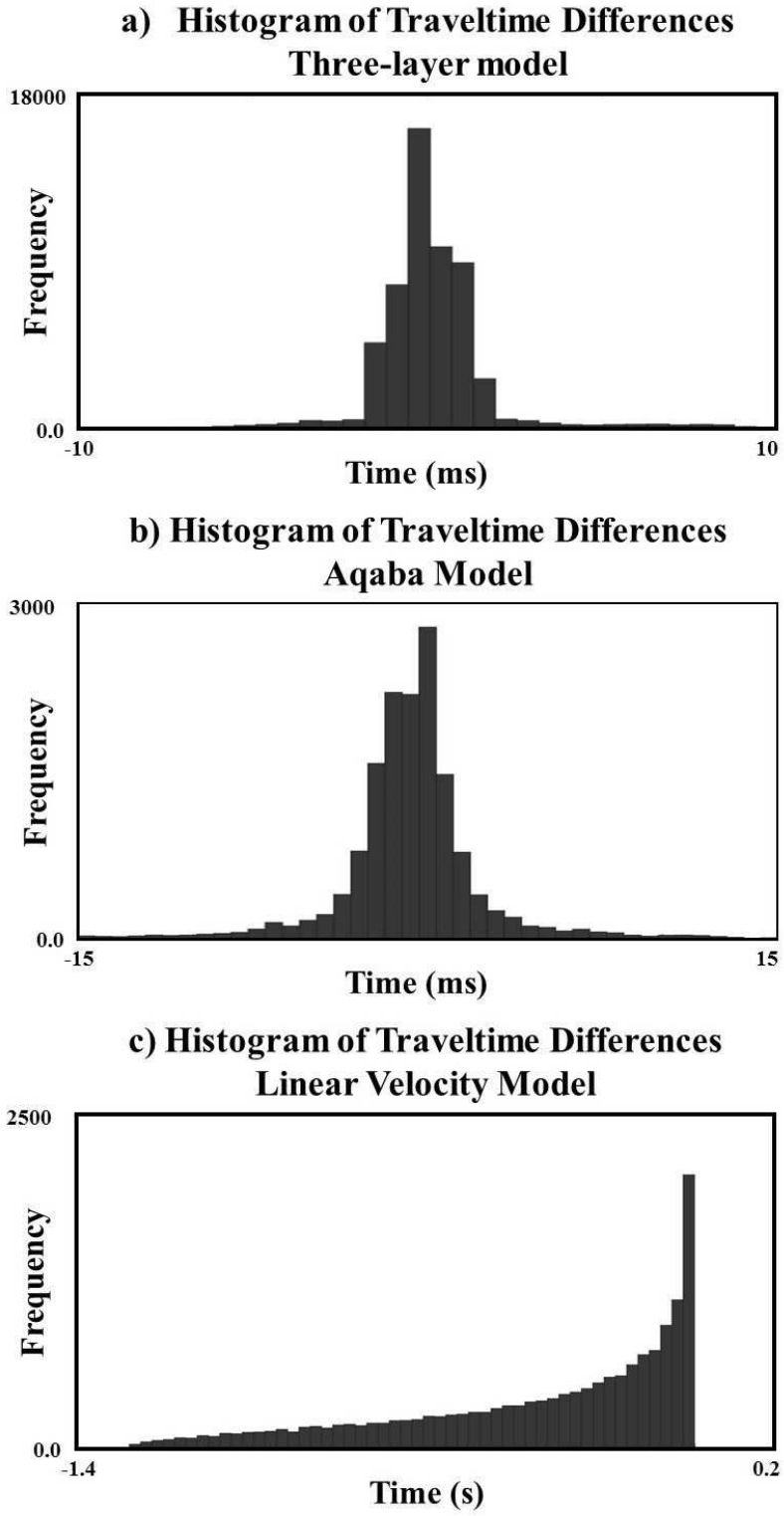

Figure 7. The histogram of the difference between true and virtual traveltimes of the a) three-layer, b) Aqaba, and c) gradient synthetic models. The differences in both a) and b) are less than 5 ms, while in c) it is as high as 1.4 s.

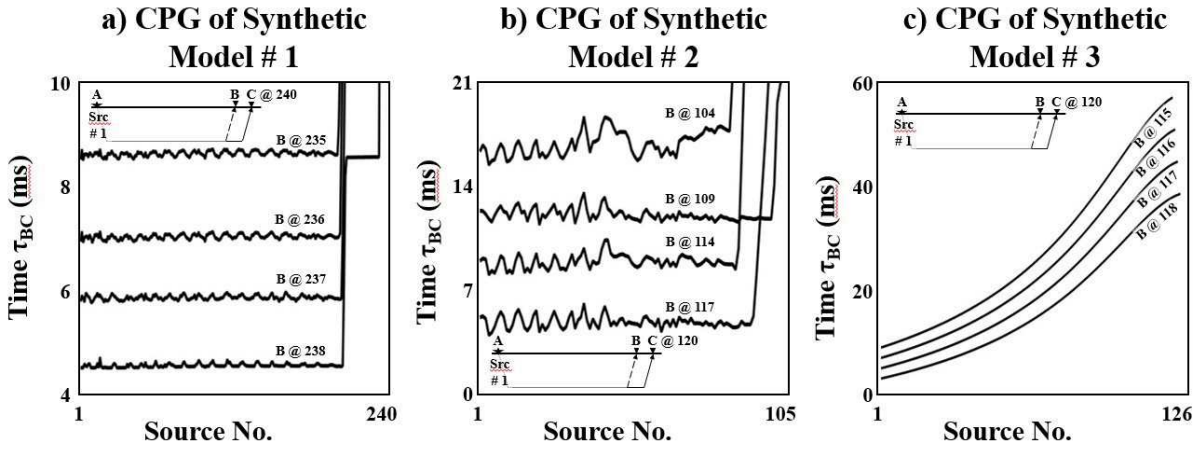

Figure 8. Consistency test results for the a) three-layer, b) Aqaba, and c) gradient synthetic models.

slope at short offsets, as illustrated in Figure 11. These unphysical traveltimes are easily identified* and eliminated, but they leave a gap in the arrival times of the direct waves. To fill in this gap, we included the direct-wave traveltimes from the 5 infill CSGs with a shot interval of 60 m. These direct-wave traveltimes were then interpolated to other source locations to fill in the missing direct-wave traveltimes in the other virtual CSGs, and the result id shown in Figure 10c. Figure 10d shows the difference between the true and the virtual traveltimes. The difference in traveltimes values are very small except near the cross-over distance. Figure 7b shows the histogram of Figure 10d.

All of the virtual traveltimes and additional direct-wave were then inverted to give the Figure 9d virtual tomogram. There is a very good agreement between the standard and virtual tomograms, which is somewhat surprising because some refraction arrivals are associated with diving waves. Figure 8b shows that the CPG traveltimes mostly agree with one another for the same CPG.

3.3 Linear Velocity Gradient Model

Traveltimes associated with pure diving waves cannot use equation 3 to generate traveltimes of virtual head waves. To demonstrate this point, we used the linear-velocity-gradient model of Figure 12 to calculate the first arrival traveltimes for 126 shot gathers with shot interval of 8 m. The calculated traveltimes are shown in Figure 13a. Then only the two reciprocal shots at x=0 and x=2 km (Figure 13b) are converted by equation 3 to virtual traveltimes for virtual shots at every gridpoint along the surface (Figure 13c). The differences between the actual and virtual traveltimes range between 0 and -1.4 s as shown in Figure 7c. This is consistent with the disagreement between the traveltime matrices in Figure 13a and Figure 13c. The reason, of course, is that the diving waves violate the head-wave assumption. Figure 8c shows that the CPG traveltimes disagree with one another, as expected for diving waves.

* The unphysical traveltimes can be visually identified by identifying sudden changes in slope. The unphysical traveltimes can automatically be eliminated by the consistency test.

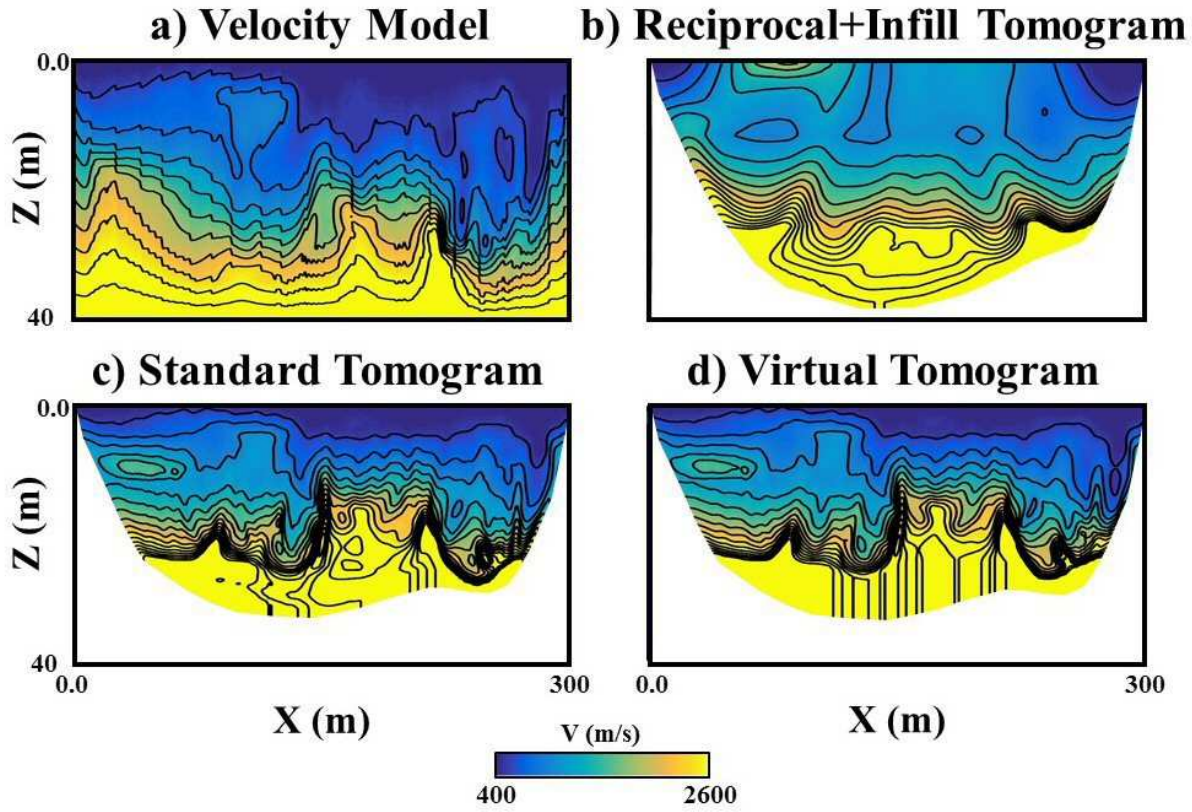

Figure 9. a) Aqaba velocity model, b) tomogram inverted from the two reciprocal and some additional direct-wave traveltimes, c) standard tomogram inverted from the $14,400$ actual traveltimes in 240 shot gathers, with a shot at each geophone location. d) Virtual tomogram inverted from virtual and interpolated direct-wave traveltimes. The Aqaba model is based on results from a seismic survey near the Gulf of Aqaba.

3.4 Aqaba Field Data

A seismic survey was carried out near the Gulf of Aqaba (Hanafy et al., 2014), where 120 vertical-component geophones were deployed at 2.5 m intervals along a line. A 90-kg accelerated-weight drop was used for a source at every geophone position to record 120 common shot gathers. A typical shot gather is shown in Figure 14a, and more than 14,000 first-arrival traveltimes were picked from the 14,400 traces in the CSGs (Figure 15c. The signal-to-noise ratio was excellent so traveltimes could be picked at almost every trace, as verified by the densely-populated traveltime matrix in Figure 15c.

A source at each end of the line was used to form two reciprocal shot gathers. The first-arrival traveltimes were picked and used to compute more than $14,000$ virtual traveltimes from equation 3. As in the synthetic example, some of these traveltimes are not physically related to refraction times because the receiver-receiver offset is not at a post-critical offset. These unphysical traveltimes are easily identified and eliminated, but they leave a gap in the arrival times of the direct waves. To fill in this gap, we included the direct-wave traveltimes from 5 infill CSGs with a shot interval of 50 m (Figure 15a).

Inverting the traveltimes by a multiscale tomography method (Nemeth et al., 1997) gives the tomograms shown in Figures 15b, 15d,

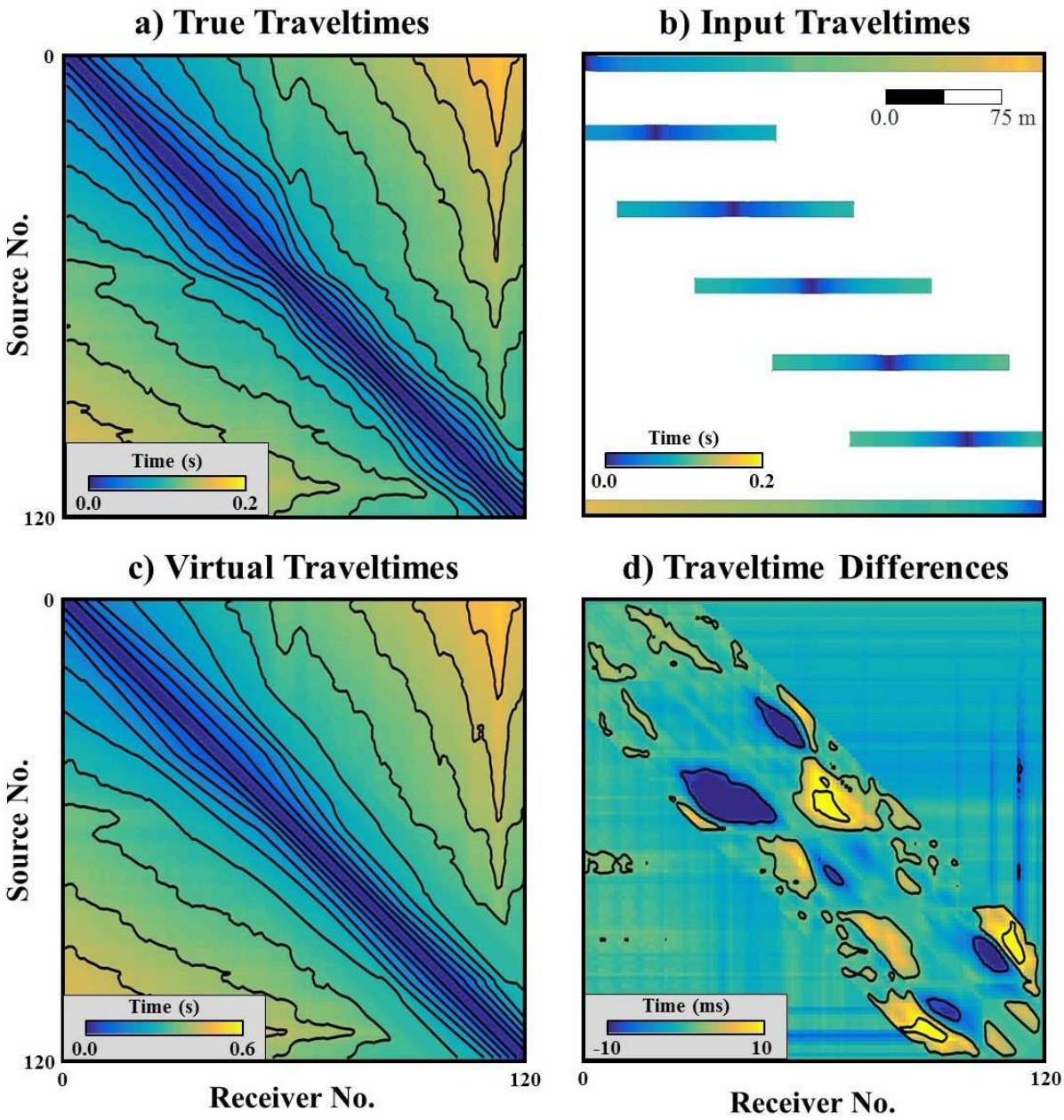

Figure 10. a) The actual traveltimes, b) two reciprocal and 5 infill shot gathers used as input to the proposed method, c) the virtual traveltimes calculated from equation 3, and d) the difference between the actual and the virtual traveltimes.

and 15f, respectively. It is clear that there is a mostly excellent agreement between the virtual and standard tomograms shown in Figures 15d and 15f, respectively. In the standard tomogram, the shooting effort required 1.5 days to conduct, and more than a day of effort was needed for picking $(14,400)$ traveltimes. For the virtual tomogram, it is estimated that less than 1 hour of shooting time would be needed and less than 30 minutes of picking time for the reciprocal and infill traveltimes. Moreover, the 5 shot gathers recorded for the direct-wave traveltimes would not require much more effort to record, because only one strike of the weight-drop source is needed to record short-offset traces with adequate SNR. The subsequent generation of the $O(14,000)$ virtual traveltimes is automatically done by the computer in less than a second.

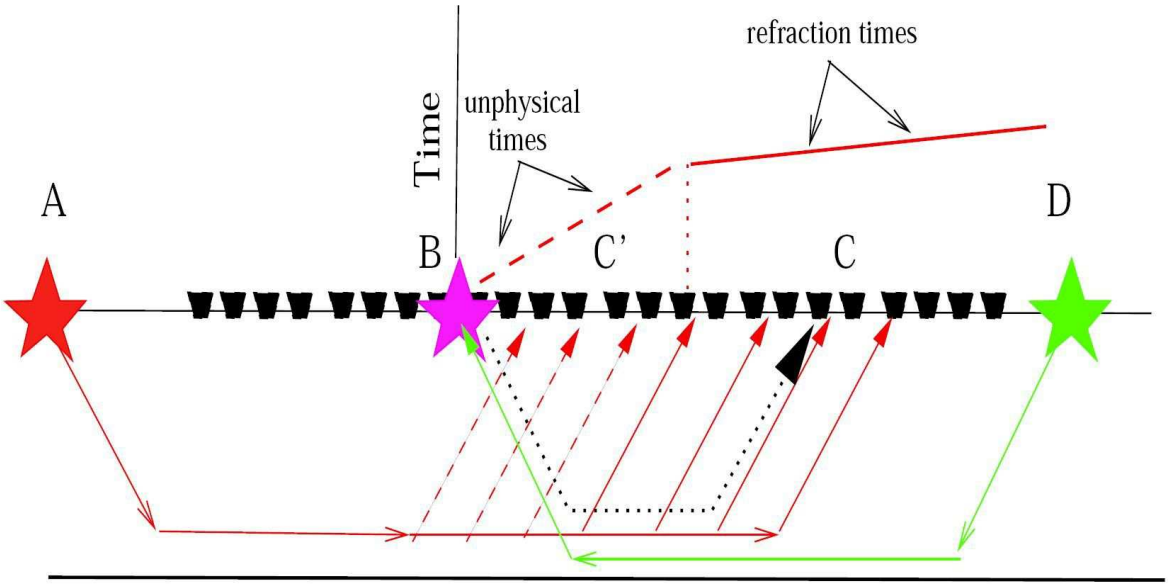

Figure 11. Ray diagram showing the dashed unphysical rays such that $\tau_{BC'} = \tau_{DB} + \tau_{AC'} - \tau_{DA}$ is an unphysical virtual traveltime which does not correspond to a physical head wave. In comparison, $\tau_{BC} = \tau_{DB} + \tau_{AC} - \tau_{DA}$ corresponds to the virtual traveltimes of a physical head wave along the dotted black rays. The zone of unphysical virtual traveltimes is between the origin at B and the sudden change in the traveltime slope.

Figure 16a shows that the differences between the virtual and actual traveltimes are well below the estimated picking error of 4 ms in the data.

The consistency test results for the recorded Aqaba data are depicted in Figure 17a. For specified locations of $\mathbf{B}$ and $\mathbf{C}$ (see ray diagram in upper right), the thin black line represents the traveltimes τ_{BC} for all actual shot locations to the left of $\mathbf{B}$. Here, the location $\mathbf{C}$ is always at location #120 and $\mathbf{B}$ is progressively moved to its left to give rise to larger traveltimes τ_{BC}.

Most of the recorded traveltimes τ_{BC} to the left are flat to within a quarter of the dominant period $\frac{1}{4}$T, and therefore indicate passage of the consistency test. However, the traveltimes associated with the bumps are rejected. This plot is for one location of $\mathbf{C}$, and so the traveltimes for other locations of $\mathbf{C}$ should also be tested for consistency with the head-wave assumption.

It is tempting to apply the consistency test to the virtual traveltimes $\tilde{\tau}_{ij}$, not just the recorded traveltimes τ_{ij}. However, this will not be useful as shown in the following exercise. Assume a reciprocal source at $\mathbf{s}$ to the left of $\mathbf{A}$ and a reciprocal source to the far right at $\mathbf{D}$ (Figure 1). The receiver locations between these two sources are at, from left to right, $\mathbf{A}$, $\mathbf{B}$ and $\mathbf{C}$. Recorded traveltimes, from two reciprocal shots at $\mathbf{s}$ and $\mathbf{D}$, are used to compute the virtual traveltimes τ_{ij} for all interior locations associated with i and j indices. These virtual traveltimes

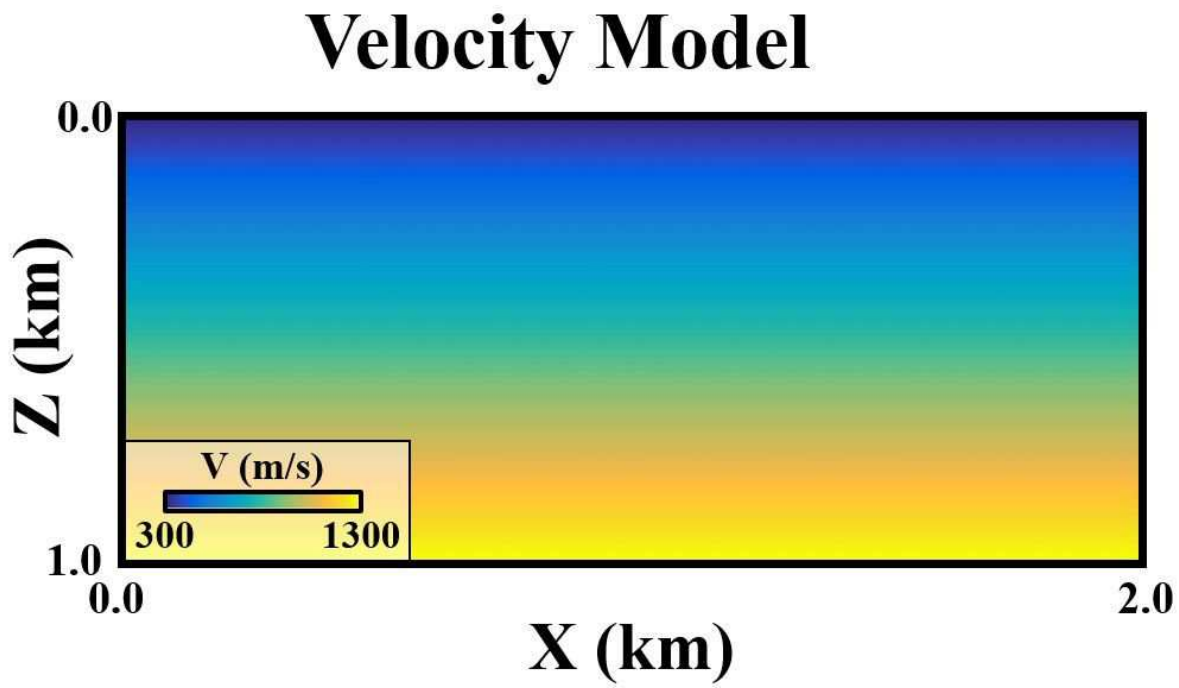

Figure 12. Model with velocity linearly increasing in depth.

are used to generate the CPG traveltime $\bar{\tau}_{BC}$ in equation 5. Plugging equation 4 into equation 5 we get

$$\begin{aligned}\bar{\tau}_{BC} &= \tilde{\tau}_{AC} - \tilde{\tau}_{AB}, \\ &= \tau_{sC} + \tau_{DA} - \tau_{sD} - [\tau_{sB} + \tau_{DA} - \tau_{sD}], \\ &= \tau_{sC} - \tau_{sB}, \end{aligned} \tag{6}$$

which is true for any postcritical location $\mathbf{A}$ to the left of $\mathbf{B}$. Even if the recorded reciprocal traveltimes are those for diving waves, the virtual CPG time $\bar{\tau}_{BC}$ will $appear$ to be a head-wave time because it is the same for any virtual source location $\mathbf{A}$ to the left of $\mathbf{B}$. Thus, the consistency test cannot be applied to $virtual$ traveltimes to distinguish head-wave arrivals from diving waves.

3.5 Wadi Qadid Field Data

A seismic survey was carried out near KAUST (Jadoon et al., 2016), where 117 vertical-component geophones were deployed at 2.0 m intervals along a line. A 90-kg accelerated-weight drop was used for a source at every geophone position to collect 117 common shot gathers. A typical shot gather is shown in Figure 14b, and more than 13,000 first-arrival traveltimes were picked from the 13,689 traces in the CSGs. The signal-to-noise ratio was excellent so traveltimes could be picked at almost every trace, as verified by the densely-populated traveltime matrix in Figure 18c.

A source at each end of the line was used to form two reciprocal shot gathers. The first-arrival traveltimes were picked and used to

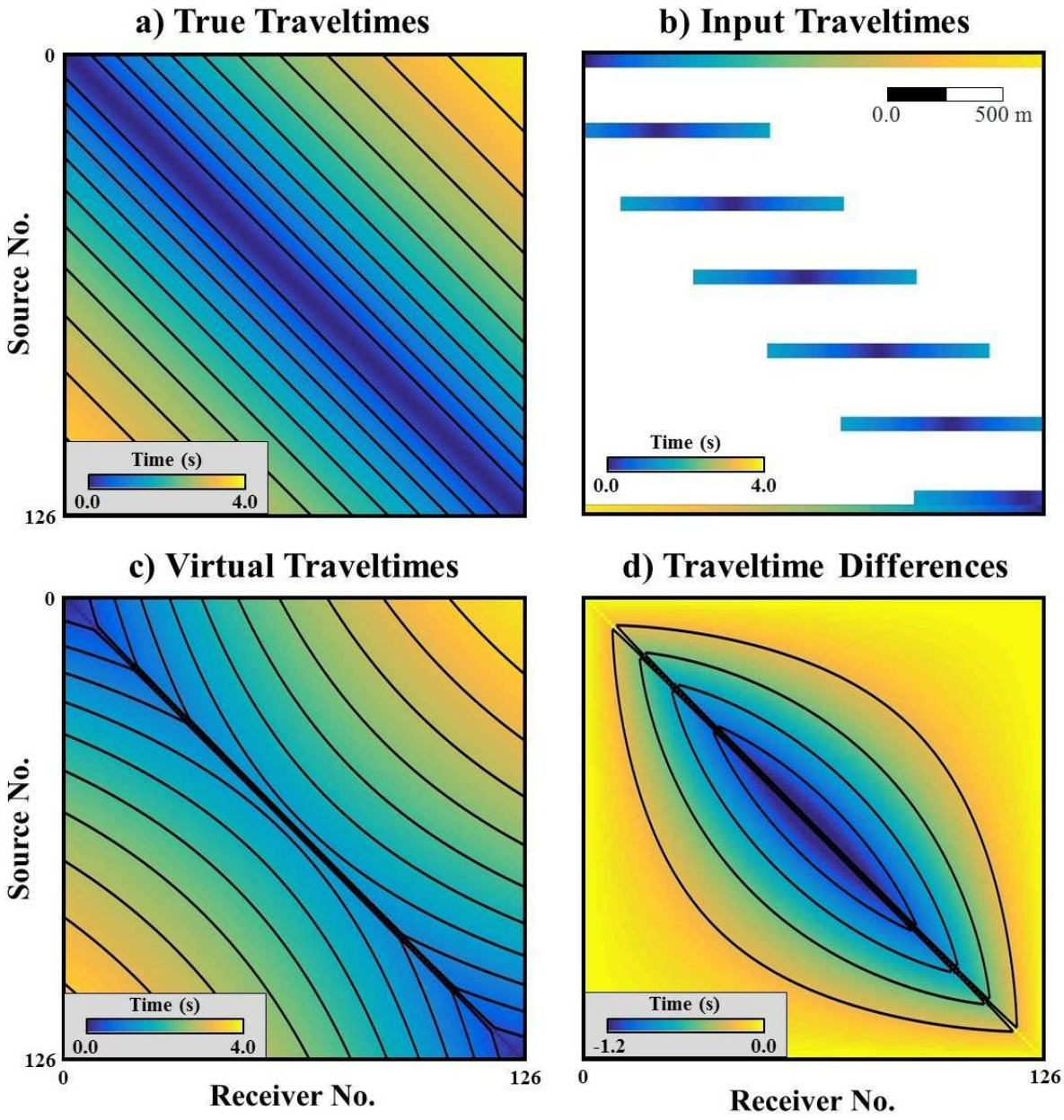

Figure 13. a) True, b) reciprocal, and c) virtual traveltimes. d) The difference between the true and virtual traveltimes.

compute $13,689$ virtual traveltimes from equation 3. As in the synthetic example, some of these traveltimes are not physically related to refraction times because the receiver-receiver offset is not at a post-critical offset. These unphysical traveltimes are easily identified and eliminated, but they leave a gap in the arrival times of the direct waves. To fill in this gap, we included the direct-wave traveltimes from 5 CSGs with a shot interval of 40 m (Figure 18a).

Similar to the Aqaba tomograms, the virtual and standard Wadi tomograms in Figures 18d and 18f mostly agree with one another. This is not too surprising because the virtual and standard traveltimes are within 1/4 T of one another, as illustrated in Figure 16b. Most of the

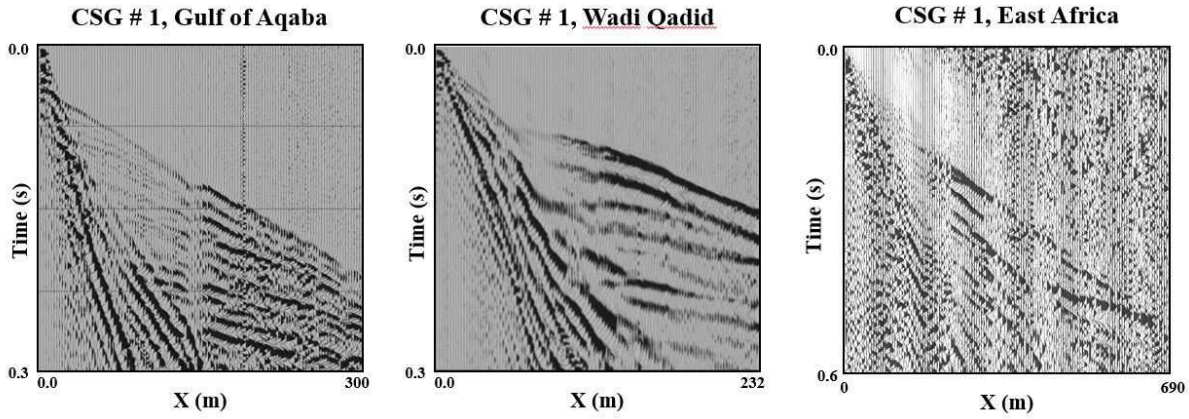

Figure 14. Typical common shot gathers recorded at the a) Aqaba, b) Wadi Qadid, and c) East Africa field sites.

recorded traveltimes passed the consistency test, as shown in Figure 17b. Similar to the Aqaba results, the Figure 18b tomogram computed from the Wadi reciprocal data largely disagrees with the "groundtruth" tomogram in Figure 18d.

3.6 East Africa Field Data

Parsimonious interferometry is now applied to a data set consisting of strong diving waves. In this case, the survey is conducted over a deep basin where the two reciprocal shots at the end of the line are separated by 690 m , and there are 139 vertical-component geophones evenly distributed along the line at 5 m intervals. The standard survey is conducted with an accelerated weight drop sources located at 10 m intervals along the line. A typical shot gather is shown in Figure 14c.

The reciprocal traveltimes are picked and used to generate the virtual traveltimes. The comparison between the reciprocal, virtual, and standard traveltimes is depicted along the left column of Figure 19. Unlike the Aqaba or Wadi Qadid data, there are noticeable discrepancies between the virtual and standard traveltimes (Figure 16c). These discrepancies are manifested in the noticeable dissimilarities between the standard and virtual tomograms in the right column. The reason for these discrepancies is revealed by the consistency test results illustrated in Figure 17c, which shows strong violations of the head-wave assumption.

4 CONCLUSIONS

The theory of parsimonious interferometry is presented where a dense set of virtual refraction traveltimes is computed from refraction traveltimes picked from a pair of reciprocal and a couple of infill shot gathers. In theory, a virtual-shot gather of traveltimes can be computed for a virtual shot at each of the geophones in the 2D reciprocal survey. This means that $O(N^2)$ of virtual traveltimes can be created from virtual shots placed at each of the N geophones. An advantage of virtual data is that it acts as a preconditioner to $\mathbf{L}^T\mathbf{L}$, which reduces the condition number by a factor of three compared to that of the reciprocal data. The accompanying increase in ray coverage reduces the size

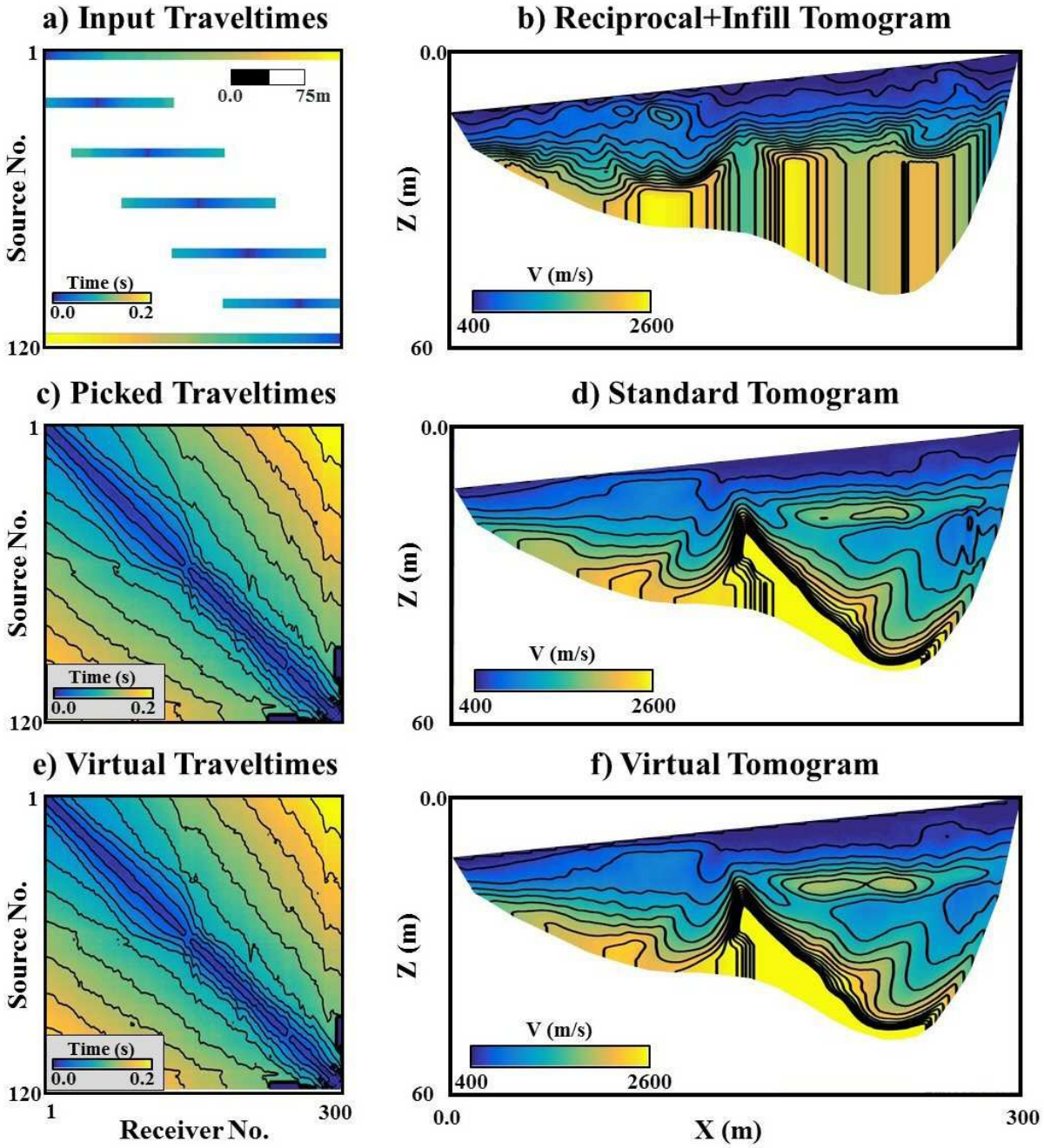

Figure 15. Gulf of Aqaba traveltime picks for the a) reciprocal, c) standard, and e) virtual field data. The corresponding tomograms are on the righthand column of figures.

of the null space solutions to the traveltime equations. In addition the slowness variance associated with virtual data can be less than that obtained from reciprocal data.

Tests with synthetic data and field data validate that inversion of virtual refraction traveltimes can give tomograms that closely resemble those computed from traveltimes recorded in a dense survey. If the first arrivals are mostly head-wave arrivals, not strong diving waves, then

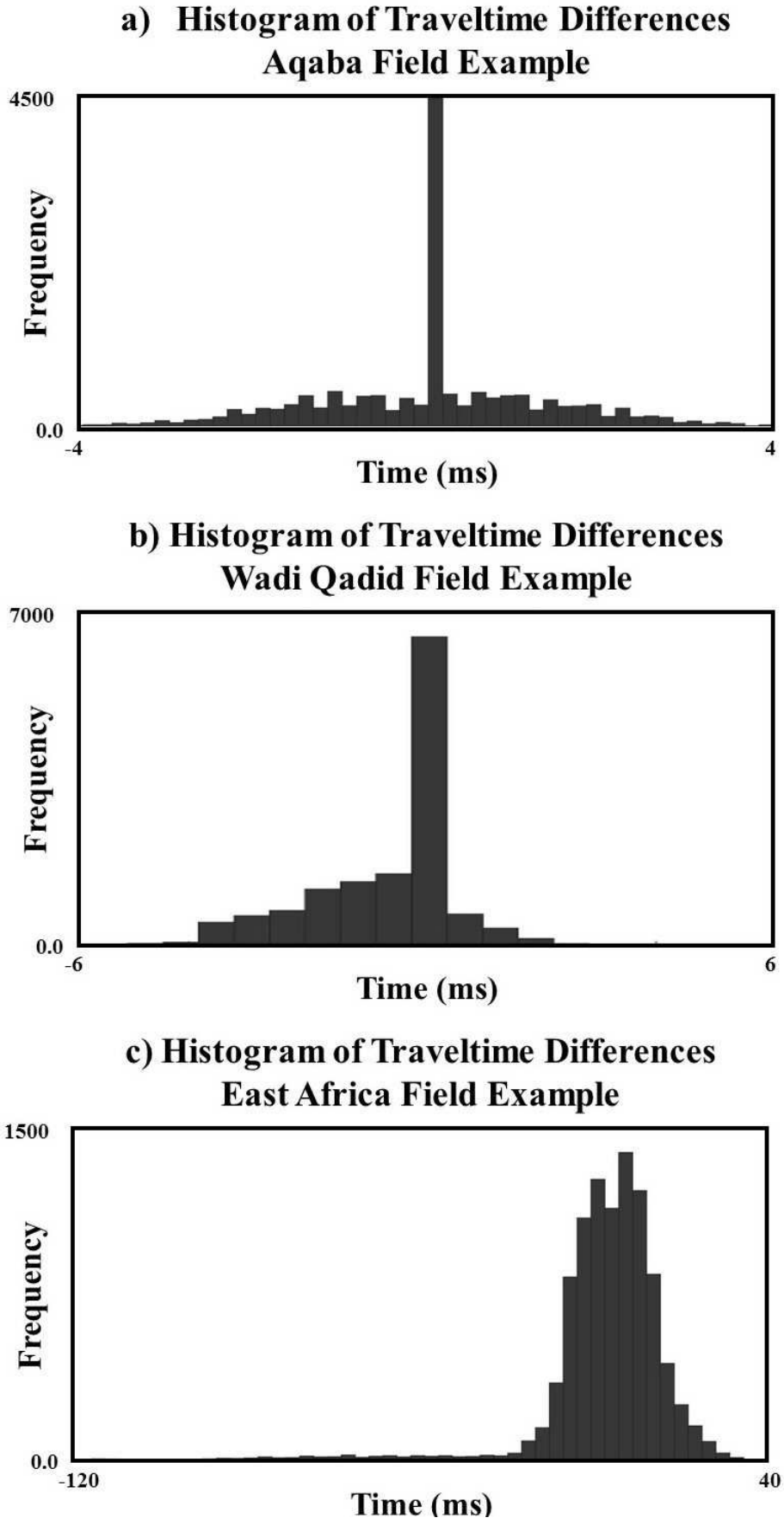

Figure 16. The histogram of the differences between the true and virtual traveltimes obtained from a) Aqaba, b) Wadi Qadid, and c) East Africa data. The differences in both a) and b) are less than 5 ms, while in c) it is as high as 120 ms.

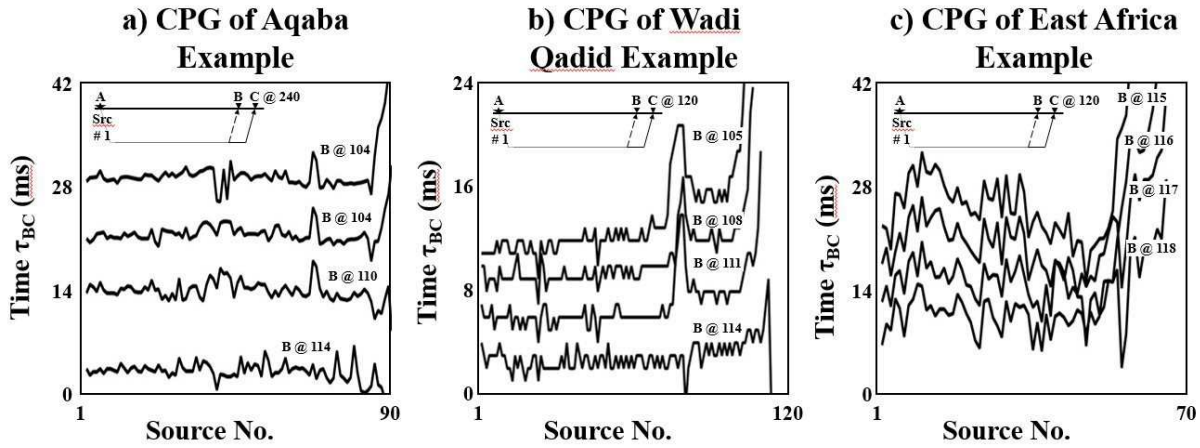

Figure 17. Consistency test results for the a) Wadi Qadid, b) Aqaba , and c) East Africa data. The East Africa data in c) fail the consistency test while it is passed at both Wadi Qadid, and Aqaba data. In all of the figures, the input data were traveltimes picked from the standard survey where there is a dense distribution of shots.

dense 2D refraction surveys might be replaced by inexpensive reciprocal surveys with as few as two shots placed at each end of the line and several infill shot gathers.

Some opportunities presented by parsimonious interferometry include the following.

(i) The virtual traveltimes can be used to design narrow picking windows for an autopicker to pick first-arrival traveltimes from the dense survey data. For example, the Aqaba data only used 240 traveltime picks to automatically generate $O(14,000)$ virtual traveltimes.

(ii) More efficient surveys can be carried out because a reciprocal survey that includes several infill shot gathers are much less time consuming than a standard survey.

(iii) Traveltimes from refractions can be used to estimate statics (Yilmaz, 2001). The problem is that land surveys have coarse spacing between recording stations and so prevent an estimate of the shallow velocity model. Can an inexpensive source truck towing a short-offset land streamer be used to quickly obtain short-offset reciprocal gathers? If so, the virtual traveltimes can be inverted to give a detailed estimate of the shallow velocity distribution. A source is required at both the front and back of the land streamer.

(iv) Refraction surveys in environmentally sensitive sites, such as archaelogical surveys, might use a parsimonious survey to minimize the number of sources.

Some limitations of parsimonious interferometry are the following.

(i) The virtual traveltimes can have three times the variance of the recorded traveltimes for random uncorrelated picking errors.

(ii) The first arrivals are assumed to be mostly head waves, which is strictly not true for velocities that strongly increase with depth.

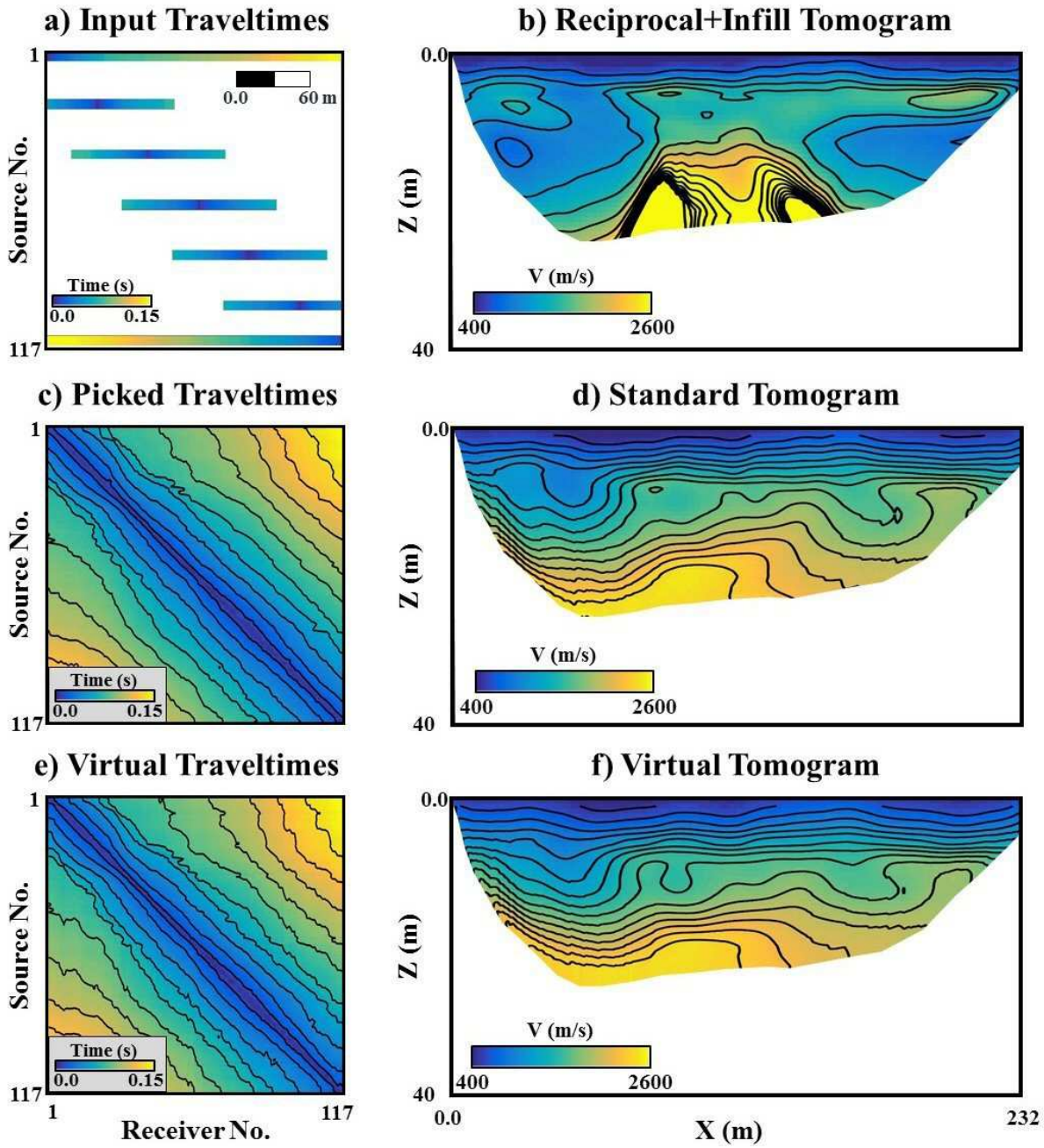

Figure 18. Wadi Qadid traveltime picks for the a) reciprocal, c) standard, and e) virtual traveltimes. The corresponding tomograms are on the righthand column of figures.

Surprisingly, our tests suggest that parsimonious tomography has some tolerance to traveltimes associated with diving waves. We don't always expect this type of tolerance for wide-offset refractions from the deep part of a basin or crust.

(iii) First-arrivals with low signal-to-noise ratios (SNRs) will contain large picking errors at far-offset traces. These large picking errors are expected to propagate to all source-receiver offsets in the virtual data.

(iv) If the reciprocal pair of shots is too far apart then this will lead to poor lateral resolution and gaps in the illumination of the subsurface.

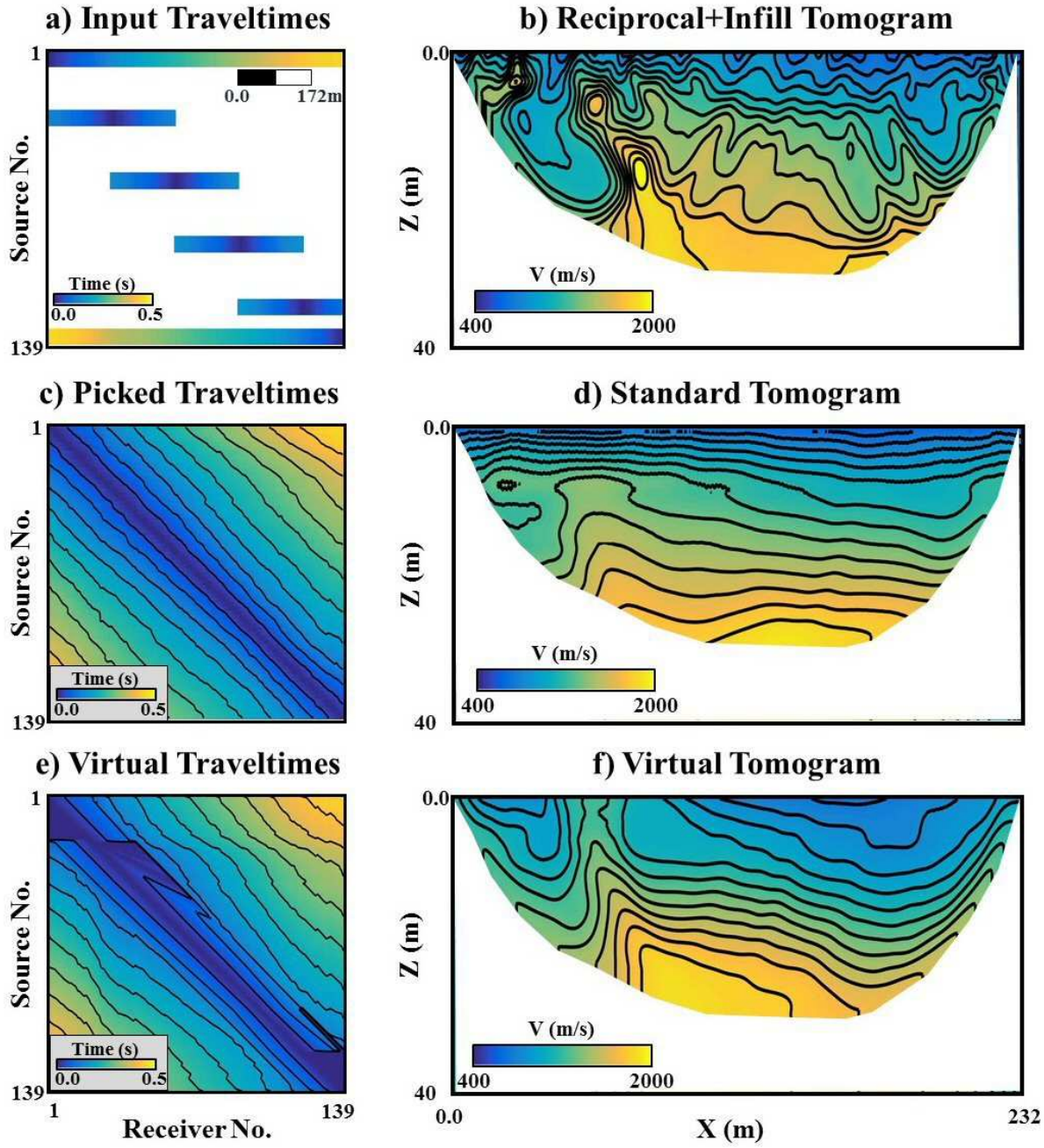

Figure 19. East Africa traveltime picks for the a) reciprocal, c) standard, and e) virtual traveltimes. The corresponding tomograms are on the righthand column of figures.

This problem can be partly mitigated by picking later direct and refraction arrivals, or by conducting additional reciprocal surveys with shorter offsets across the survey area.

(v) Out-of-the-plane refractions in the reciprocal survey will degrade the accuracy of the virtual refractions.

(vi) The recorded first-arrival traveltimes must satisfy the consistency assumption, which is difficult if only two reciprocal shot gathers are recorded. One possibility is to examine these two reciprocal gathers for evidence of head waves, where first arrivals have the same slope

for a large range of source-receiver offsets. Diving waves might be recognized by the slope dt/dx continuously decreasing with increasing offset. Alternatively, one can record some extra shots in the interior over a portion of the line and test the traveltimes from these shot gathers for consistency.

5 APPENDIX I: CONDITION NUMBER OF $[\mathbf{L}^T\mathbf{L}]$

We will derive the formulas for the condition number κ of the $[\mathbf{L}^T\mathbf{L}]$ associated with the reciprocal and virtual-traveltime equations. The traveltimes are for the refractions in the Figure 20 slowness model. By definition, the 1-norm condition number is

$$\kappa(\mathbf{L}^T\mathbf{L}) = ||[\mathbf{L}^T\mathbf{L}]||\ ||[\mathbf{L}^T\mathbf{L}]^{-1}||,$$

$$= \{max_j \sum_{i=1}^{N} |[\mathbf{L}^T\mathbf{L}]_{ij}|\}\{max_j \sum_{i=1}^{N} |[\mathbf{L}^T\mathbf{L}]^{-1}_{ij}|\}. \quad (7)$$

5.1 κ^{recip} for Reciprocal Data

Assume the two-layer model in Figure 20, where the second layer has lateral heterogeneities with an unknown slowness s_i in each of the square boxes. The slowness of the top layer is homogeneous and is assumed to be known, the thickness of this top layer is also known, and each box has a width of l. The goal is to estimate the condition number of $[\mathbf{L}^T\mathbf{L}]$ associated with the reciprocal refraction traveltimes where a source is located at each end of the model.

The traveltime equations for a shot at position 0 in Figure 20a and one at X=5 can be represented by $\mathbf{Ls} = \mathbf{t}$, where

$$\mathbf{Ls} = \begin{bmatrix} l & 0 & 0 & 0 & 0 \\ l & l & 0 & 0 & 0 \\ l & l & l & 0 & 0 \\ l & l & l & l & 0 \\ l & l & l & l & l \\ 0 & 0 & 0 & 0 & l \\ 0 & 0 & 0 & l & l \\ 0 & 0 & l & l & l \\ 0 & l & l & l & l \\ l & l & l & l & l \end{bmatrix} \begin{pmatrix} s_1 \\ s_2 \\ s_3 \\ s_4 \\ s_5 \end{pmatrix} = \begin{pmatrix} t_1 \\ t_2 \\ t_3 \\ t_4 \\ t_5 \\ \tilde{t}_1 \\ \tilde{t}_2 \\ \tilde{t}_3 \\ \tilde{t}_4 \\ \tilde{t}_5 \end{pmatrix} = \mathbf{t}, \quad (8)$$

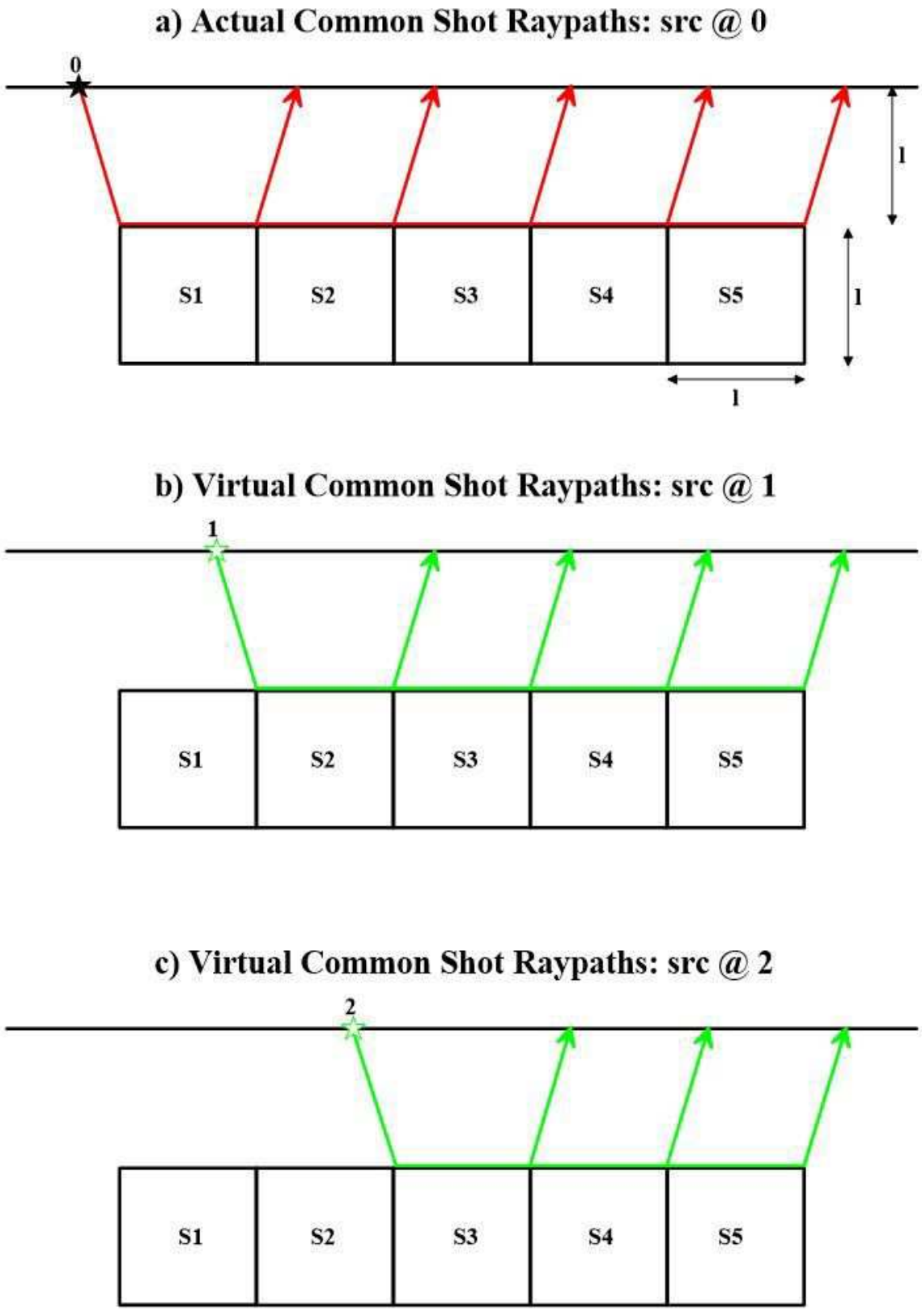

Figure 20. Raypaths for a common shot gather with the source at positions a) 0, b) 1, and c) 2. Here, it is assumed that the source at position 0 is an actual source and the sources at 1 and 2 are virtual sources generated from a reciprocal pair of shot gathers.

where t_i ($\tilde{t}_i$) is the traveltime for a rightgoing (leftgoing) refraction along a horizontal raypath. The traveltimes t_i and $\tilde{t}_i$ are considered to be the recorded traveltimes after subtracting the upgoing and downgoing traveltimes in the top layer, which are assumed to be known.

The $\mathbf{L}$ matrix can be decomposed into

$$\mathbf{L} = \begin{bmatrix} \mathbf{L}_0 \\ \bar{\mathbf{L}}_0 \end{bmatrix}, \tag{9}$$

where

$$\mathbf{L}_0 = l\mathbf{Q} = l \begin{bmatrix} 1 & 0 & 0 & 0 & 0 \\ 1 & 1 & 0 & 0 & 0 \\ 1 & 1 & 1 & 0 & 0 \\ 1 & 1 & 1 & 1 & 0 \\ 1 & 1 & 1 & 1 & 1 \end{bmatrix}; \quad \bar{\mathbf{L}}_0 = l\mathbf{Q} \begin{bmatrix} 0 & 0 & 0 & 0 & 1 \\ 0 & 0 & 0 & 1 & 0 \\ 0 & 0 & 1 & 0 & 0 \\ 0 & 1 & 0 & 0 & 0 \\ 1 & 0 & 0 & 0 & 0 \end{bmatrix}, \tag{10}$$

where the inverse to $\mathbf{Q}$ is the backward difference matrix (Schuster, 1988)

$$\mathbf{Q}^{-1} = \begin{bmatrix} 1 & 0 & 0 & 0 & 0 \\ -1 & 1 & 0 & 0 & 0 \\ 0 & -1 & 1 & 0 & 0 \\ 0 & 0 & -1 & 1 & 0 \\ 0 & 0 & 0 & -1 & 1 \end{bmatrix}. \tag{11}$$

Therefore the normal matrix $[\mathbf{L}^T\mathbf{L}] = \mathbf{L}_0^T\mathbf{L}_0 + \bar{\mathbf{L}}_0^T\bar{\mathbf{L}}_0$ is

$$[\mathbf{L}^T\mathbf{L}] = l^2 \begin{bmatrix} 6 & 5 & 4 & 3 & 2 \\ 5 & 6 & 5 & 4 & 3 \\ 4 & 5 & 6 & 5 & 4 \\ 3 & 4 & 5 & 6 & 5 \\ 2 & 3 & 4 & 5 & 6 \end{bmatrix}. \tag{12}$$

and its inverse is

$$[\mathbf{L}^T\mathbf{L}]^{-1} = \frac{1}{l^2} \begin{bmatrix} 0.5625 & -0.5 & 0 & 0 & 0.0625 \\ -0.5 & 1.0 & -0.5 & 0 & 0 \\ 0 & -0.5 & 1.0 & -0.5 & 0 \\ 0 & 0 & -0.5 & 1.0 & -0.5 \\ 0.0625 & 0 & 0 & -0.5 & 0.5625 \end{bmatrix}. \tag{13}$$

In general the normal matrix $[\mathbf{L}^T\mathbf{L}]$ for $2N$ reciprocal equations is the Toeplitz matrix

$$[\mathbf{L}^T\mathbf{L}] = l^2 \begin{bmatrix} N+1 & N & N-1 & . & . & . & . & 3 & 2 \\ N & N+1 & N & N-1 & . & . & . & . & 3 \\ N-1 & N & N+1 & N & . & . & . & . & . \\ N-2 & N-1 & N & N+1 & . & . & . & . & . \\ . & . & . & . & \ddots & . & . & . & . \\ . & . & . & . & . & . & . & . & . \\ . & . & . & . & . & . & N+1 & N & N-1 \\ 3 & . & . & . & . & . & N & N+1 & N \\ 2 & 3 & . & . & . & . & N-1 & N & N+1 \end{bmatrix}, \tag{14}$$

which is defined as

$$[\mathbf{L}^T\mathbf{L}]_{ij} = l^2 \begin{bmatrix} N+1-(j-i) & i \leq j \\ N+1-(i-j) & i > j. \end{bmatrix} \tag{15}$$

Therefore, for even values of N, the 1-norm of the normal matrix for reciprocal data is

$$\begin{aligned} max_j \sum_{i=1}^{N} |[\mathbf{L}^T\mathbf{L}]_{ij}| &= \sum_{i=1}^{N} |[\mathbf{L}^T\mathbf{L}]_{i\frac{N}{2}}|, \\ &= l^2\{\sum_{i=1}^{N/2}[N/2+1+i] + \sum_{i=N/2+1}^{N}[3N/2+1-i]\}, \\ &= l^2[\frac{3N^2}{4}+N]. \end{aligned} \tag{16}$$

The inverse matrix for equation 14 is

$$[\mathbf{L}^T\mathbf{L}]^{-1} = \frac{1}{l^2}\begin{bmatrix} \alpha & -0.5 & 0 & 0 & \dots & 0 & \beta \\ -0.5 & 1 & -0.5 & 0 & \dots & 0 & 0 \\ 0 & -0.5 & 1 & -0.5 & \dots & 0 & 0 \\ \vdots & \vdots & \ddots & \ddots & \ddots & \vdots & \vdots \\ . & . & . & . & . & . & . \\ . & . & . & -0.5 & 1 & -0.5 & 0 \\ 0 & 0 & \dots & 0 & -0.5 & 1 & -0.5 \\ \beta & 0 & \dots & 0 & 0 & -0.5 & \alpha \end{bmatrix}, \tag{17}$$

where $\alpha = \frac{0.5N+2}{N+3}$ and $\beta = -\frac{\alpha N}{3} + \frac{0.5(N+1)}{3}$ for $N \geq 3$. The 1-norm of this inverse is

$$max_j \sum_{i=1}^{N} |[\mathbf{L}^T\mathbf{L}]^{-1}_{ij}| = \frac{2}{l^2}. \tag{18}$$

Substituting equations 16 and 18 into equation 7 gives the condition number for the reciprocal traveltimes equations:

$$\kappa(\mathbf{L}^T\mathbf{L})^{recip} \quad = \quad \frac{3N^2}{2} + 2N, \tag{19}$$

so that $\kappa(\mathbf{L}^T\mathbf{L})^{recip}$ grows quadratically with the number of unknowns N.

5.2 κ^{virt} for Virtual Data

We will now derive the condition number $\kappa^{virt} = N^2/2 + N$ for the $\mathbf{L}^T\mathbf{L}$ from virtual data, which is about 3 times smaller than that for reciprocal data. This suggests that there will be many fewer slowness models that satisfy the noisy virtual data compared to the reciprocal data.

As discussed previously, virtual refraction traveltimes can be created from the reciprocal traveltimes. Thus, the virtual-traveltime equa-

tions for the raypaths depicted in Figure 1b for a virtual source at position 1 are given by

$$\mathbf{L}_1\mathbf{s} = l \begin{bmatrix} 0 & 0 & 0 & 0 & 0 \\ 0 & 1 & 0 & 0 & 0 \\ 0 & 1 & 1 & 0 & 0 \\ 0 & 1 & 1 & 1 & 0 \\ 0 & 1 & 1 & 1 & 1 \end{bmatrix} \begin{pmatrix} s_1 \\ s_2 \\ s_3 \\ s_4 \\ s_5 \end{pmatrix} = \begin{pmatrix} t'_1 \\ t'_2 \\ t'_3 \\ t'_4 \\ t'_5 \end{pmatrix} = \mathbf{t}_1, \tag{20}$$

where $\mathbf{t}_1$ is the vector of virtual traveltimes. In this case $\mathbf{L}_1$ can be decomposed into the product of the summation $\mathbf{Q}$ matrix in equation 10 and the column-mask matrix $\mathbf{M}_1$:

$$\mathbf{L}_1 = l\mathbf{Q}\mathbf{M}_1 = l\mathbf{Q} \begin{bmatrix} 0 & 0 & 0 & 0 & 0 \\ 0 & 1 & 0 & 0 & 0 \\ 0 & 0 & 1 & 0 & 0 \\ 0 & 0 & 0 & 1 & 0 \\ 0 & 0 & 0 & 0 & 1 \end{bmatrix}. \tag{21}$$

The role of the column-mask matrix $\mathbf{M}_i$ is to mask columns $(1, 2, \ldots\ i)$ of $\mathbf{Q}$.

In general, for N unknown slowness cells, N virtual-shot gathers can be created similar to those shown in Figure 20. The picked traveltimes give rise to the overdetermined system of equations

$$l \begin{bmatrix} \mathbf{Q}\mathbf{M}_0 \\ \mathbf{Q}\mathbf{M}_1 \\ . \\ . \\ . \\ \mathbf{Q}\mathbf{M}_{N-1} \end{bmatrix} \mathbf{s} = \begin{pmatrix} \mathbf{t}_0 \\ \mathbf{t}_1 \\ . \\ . \\ . \\ \mathbf{t}_{N-1} \end{pmatrix}. \tag{22}$$

The above system of equations lead to the $N \times N$ normal equations

$$\overbrace{l^2[\sum_{i=0}^{N-1} \mathbf{M}_i^T\mathbf{Q}^T\mathbf{Q}\mathbf{M}_i]\,\mathbf{s}}^{\mathbf{L}^T\mathbf{L}} \quad = \quad \overbrace{l\sum_{i=0}^{N-1} \mathbf{M}_i^T\mathbf{Q}^T\,\mathbf{t}_i}^{\mathbf{L}^T}, \tag{23}$$

where $[\mathbf{L}^T\mathbf{L}]$ is the symmetric matrix

$$[\mathbf{L}^T\mathbf{L}] = l^2 \begin{bmatrix} N & N-1 & N-2 & . & . & . & . & . & . & . \\ N-1 & 2(N-1) & 2(N-2) & . & . & . & . & . & . & . \\ N-2 & 2(N-2) & 3(N-2) & . & . & . & . & . & . & . \\ N-3 & 2(N-3) & 3(N-3) & . & . & . & . & . & . & . \\ . & . & . & . & . & . & . & . & . & . \\ . & . & . & . & . & . & . & . & . & . \\ . & . & . & . & . & . & . & 2(N-2) & N-2 & \\ 2 & . & . & . & . & . & . & 2(N-1) & N-1 & \\ 1 & . & . & . & . & . & . & N-1 & N & \end{bmatrix}, \tag{24}$$

which is also classified as a bisymmetric matrix (Tao and Yasuda, 2002), where one symmetry axis is along the matrix diagonal and the other is along the axis that intersects the bottom left and top right of the matrix. In this case

$$[\mathbf{L}^T\mathbf{L}]_{ij} = i(N-j+1) \;\; for\, i \le j; \;\; [\mathbf{L}^T\mathbf{L}]_{ij} = j(N-i+1) \;\; for\, i > j. \tag{25}$$

Therefore, the formula for the 1-norm of $[\mathbf{L}^T\mathbf{L}]$ is

$$\begin{aligned} ||\mathbf{L}^T\mathbf{L}|| = max_j \sum_{i=1}^{N} [\mathbf{L}^T\mathbf{L}]_{ij} &= \sum_{i=1}^{N} [\mathbf{L}^T\mathbf{L}]_{i\frac{N}{2}}, \\ &= l^2 \sum_{i=1}^{\frac{N}{2}} i(\frac{N}{2}+1) \; + \; l^2 \sum_{i=\frac{N}{2}+1}^{N} \frac{N}{2}(N-i+1), \\ &= l^2(\frac{N}{2}+1)\sum_{i=1}^{\frac{N}{2}} i \; + \; l^2 \frac{N}{2} \sum_{i=1}^{\frac{N}{2}} i, \\ &= l^2 \frac{N}{4}(N+1)(1+\frac{N}{2}), \end{aligned} \tag{26}$$

where the maximum column sum is at $j = N/2$ for N an even number.

To determine $||[\mathbf{L}^T\mathbf{L}]^{-1}||$, we need the analytic inverse of equation 24:

$$[\mathbf{L}^T\mathbf{L}]^{-1} = l^{-2}[\sum_{i=0}^{N-1} \mathbf{M}_i^T\mathbf{Q}^T\mathbf{Q}\mathbf{M}_i]^{-1}, \tag{27}$$

where

$$[\mathbf{L}^T\mathbf{L}]^{-1} = \frac{1}{l^2}\begin{bmatrix} \frac{2}{N+1} & -\frac{1}{N+1} & 0 & 0 & 0 & \dots & . & . & . \\ -\frac{1}{N+1} & \frac{2}{N+1} & -\frac{1}{N+1} & 0 & 0 & \dots & . & . & . \\ 0 & -\frac{1}{N+1} & \frac{2}{N+1} & -\frac{1}{N+1} & 0 & \dots & . & . & . \\ 0 & 0 & -\frac{1}{N+1} & \frac{2}{N+1} & -\frac{1}{N+1} & \dots & . & . & . \\ \vdots & \vdots & \vdots & \vdots & \vdots & \ddots & \vdots & \vdots & \vdots \\ . & . & . & . & . & . & . & . & . \\ . & . & . & . & . & . & . & . & . \\ . & . & . & . & 0 & 0 & -\frac{1}{N+1} & \frac{2}{N+1} & -\frac{1}{N+1} \\ . & . & . & . & 0 & 0 & 0 & -\frac{1}{N+1} & \frac{2}{N+1} \end{bmatrix}. \tag{28}$$

Thus, the 1-norm of $[\mathbf{L}^T\mathbf{L}]^{-1}$ is

$$||[\mathbf{L}^T\mathbf{L}]^{-1}|| \;=\; max_j \sum_{i=1}^{N} [\mathbf{L}^T\mathbf{L}]^{-1}_{ij} \;=\; \frac{4l^{-2}}{N+1}. \tag{29}$$

Inserting equations 26 and 29 into the definition of the 1-norm condition number gives

$$\begin{aligned} \kappa([\mathbf{L}^T\mathbf{L}])^{virt} &= ||[\mathbf{L}^T\mathbf{L}]||\;||[\mathbf{L}^T\mathbf{L}]^{-1}||, \\ &= N(1+\frac{N}{2}). \end{aligned} \tag{30}$$

Therefore, the ratio of the condition numbers in equations 30 and 19 is

$$r = \frac{\kappa^{recip}}{\kappa^{virt}} \;=\; \frac{3N+4}{N+2}, \tag{31}$$

where $r \rightarrow 3$ for large N. This says that for the large N the condition number of the reciprocal data is three times worse than that for the virtual data.

Figure 21 illustrates this fact by plotting the condition numbers associated with the reciprocal (red stars) and virtual (green stars) shot gathers. Thus, the traveltime misfit function for reciprocal traveltimes will be more characterized by contours associated with long narrow valleys. Unlike virtual-traveltime tomography, reciprocal tomography will suffer from a greater range of velocity models that can explain nearly the same data.

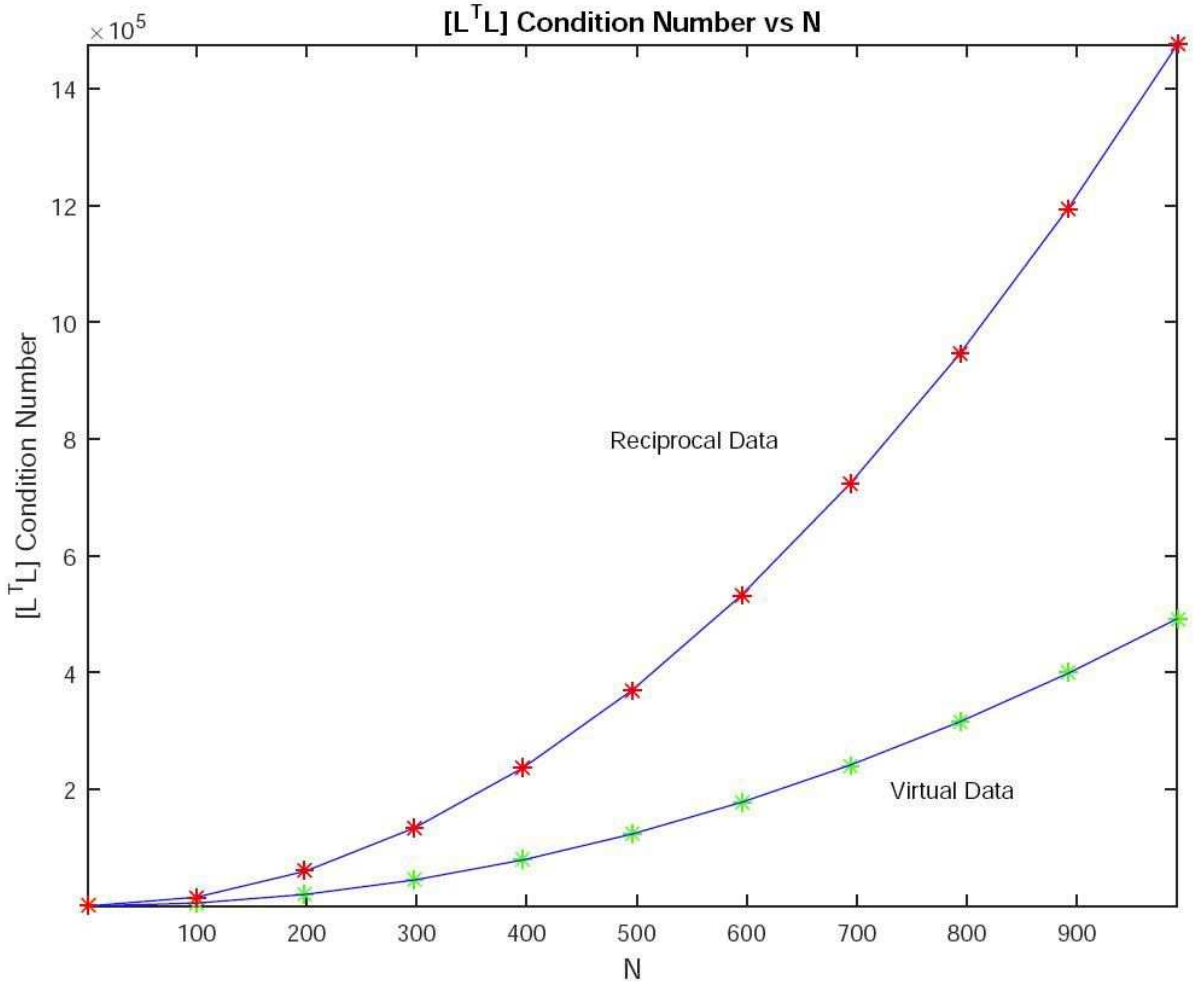

Figure 21. Condition number vs N computed from the 1-norm product $|||[\mathbf{L}^T\mathbf{L}]|| \cdot |||[\mathbf{L}^T\mathbf{L}]^{-1}||$, where $[\mathbf{L}^T\mathbf{L}]$ is the $N \times N$ normal matrix numerically computed by a MATLAB code. The red (green) stars denote the condition numbers numerically computed for the reciprocal (virtual) data associated with the checkerboard model in Figure 20. The blue lines, computed with equations 30 and 19, are in perfect agreement with the numerically computed condition numbers.

6 APPENDIX II: SLOWNESS VARIANCE

(Menke, 1984) shows that the variance of the slowness σ_i^2 in the i^{th} cell is equal to $\Sigma^2[\mathbf{L}^T\mathbf{L}]^{-1}$ if the data errors are uncorrelated zero-mean random variables with variance Σ^2. Therefore, the diagonal component of equation 28 is the virtual slowness $\bar{\sigma}_i^2$:

$$\bar{\sigma}_i^2 = \frac{\bar{\Sigma}^2}{l^2}\frac{2}{N+1}, \tag{32}$$

where $\bar{\Sigma}^2 = 3\Sigma^2$ is the variance of the virtual data†. For large N, $\bar{\sigma}_i^2$ can be significantly less than slowness variance σ_i^2 associated with the reciprocal data:

$$\sigma_i^2 \quad = \quad \frac{\sigma^2}{l^2}, \tag{33}$$

which follows from the diagonal component of the reciprocal inverse matrix in equation 17.

However, the formula in equation 32 that relates data variance to slowness variance assumes that the data are uncorrelated, which is not true for the virtual traveltimes computed with equation 3. This is because the random errors in the virtual traveltimes are correlated with one another even though the traveltime errors in the reciprocal traveltimes are uncorrelated. For example, define the reciprocal traveltime error as $\bar{\tau}_{ij}$ associated with the i^{th} source and j^{th} receiver, where the "bar" indicates a traveltime picking error. In this case the reciprocal-traveltime errors are uncorrelated, i.e., $< \bar{\tau}_{ij}\bar{\tau}_{i'j'} > \propto \delta_{ii'}\delta_{jj'}$, but the virtual-traveltime errors $< \delta\bar{\tau}_{CB}\delta\bar{\tau}_{CB'} > = < \bar{\tau}_{AC}^2 > \neq 0$ are correlated, where B' is to the left of B for the virtual-traveltime errors $\delta\bar{\tau}_{ij}$. Here, $< \ >$ represents the averaging operation over the random variables.

REFERENCES

Bishop, T. N., K. P. Bube, R. T. Cutler, R. T. Langan, P. L. Love, J. R. Resnick, R. T. Shuey, D. A. Spindler, and H. W. Wyld, 1985, Tomographic determination of velocity and depth in laterally varying media: Geophysics, **50**, 903–923.

Dong, S., J. Sheng, and G. T. Schuster, 2006, Theory and practice of refraction interferometry: SEG Expanded Abstracts, 3021–3025.

Hanafy, S. M., S. Jonsson, and Y. Klinger, 2014, Imaging normal faults in alluvial fans using geophysical techniques: Field example from the coast of gulf of aqaba, saudi arabia: SEG Technical Program Expanded Abstracts, 4670–4674.

Jadoon, K. Z., S. Al-Mashharawi, S. M. Hanafy, G. T. Schuster, and T. M. Missimer, 2016, Anthropogenic-induced changes in the mechanism of drylands ephemeral stream recharge, western saudi arabia: Water (MDPI), **8**, 14 p.

Menke, W., 1984, Geophysical data analysis: Discrete inverse theory: Academic Press Inc.

Nemeth, T., E. Normark, and F. Qin, 1997, Dynamic smoothing in crosswell traveltime tomography: Geophysics, **62**, 168–176.

Prodehl, C. and W. D. Mooney, 2012, Exploring the earths crust: history and results of controlled-source seismology: Geological Soc. Am. Mem.

Qin, F., Y. Luo, K. B. Olsen, W. Cai, and G. T. Schuster, 1992, Finite-difference solution of the eikonal equation along expanding wavefronts: Geophysics, **57**, 478–487.

Schuster, G. T., 1988, An analytic generalized inverse for common depth point and vertical seismic profile traveltime equations: Geophysics, **53**, 314–325.

———, 2005, Fermat's interferometric principle for target-oriented traveltime tomography: Geophysics, **70**, U47–U50.

Schuster, G. T., Y. Huang, M. Zhou, J. Yu, S. M. Hanafy, O. Alhagan, and W. Dai, 2014, Review on improved seismic imaging with closure phase: Geophysics, **79**, W11–W25.

† Each virtual traveltime is computed by adding two traveltimes and subtracting one traveltime. If the traveltime errors are uncorrelated and zero-mean random variables this means that the variance $\bar{\Sigma}^2$ of the virtual traveltime is 3 times the variance Σ^2 of the original data.

Snieder, R., 2004, Extracting the green's function from the correlation of coda waves: A derivation based on stationary phase: Phy. Rev. E, **69**, 046610–1 – 046610–8.

Stein, S. and M. Wyession, 2003, An introduction to seismology, earthquakes, and earth structure: Blackwell Publishing Company.

Tao, D. and M. Yasuda, 2002, A spectral characterization of generalized real symmetric centrosymmetric and generalized real symmetric skew-centrosymmetric matrices: SIAM J. Matrix Anal. Appl., **23**, 885–895.

Wapenaar, K., 2004, Retrieving the electrodynamic green's function of an arbitrary inhomogeneous medium by cross-correlation: Physical Review Letters, **93**, 254301–4.

Yilmaz, O., 2001, Seismic data analysis: SEG Publishing, Tulsa, OK.

———, 2015, Engineering seismology with applications to geotechnical engineering: SEG Publishing, Tulsa, OK.